Microturbulence in the electron cyclotron frequency range at perpendicular supercritical shocks

Laurent Muschietti, Bertrand Lembège

JOURNAL OF GEOPHYSICAL RESEARCH: SPACE PHYSICS, VOL. 118, 2267–2285, doi:10.1002/jgra.50224, 2013

Microturbulence in the electron cyclotron frequency range at perpendicular supercritical shocks

L. Muschietti[1,2] and B. Lembège[2]

Received 21 November 2012; revised 1 February 2013; accepted 10 March 2013; published 31 May 2013.

[1] Supercritical perpendicular collisionless shocks are characterized by a fraction of the incoming ions being reflected at the steep front. These reflected ions accumulate and form a foot, where the relative drift of the reflected ion beam versus the electrons can easily excite an electron cyclotron drift instability (ECDI). Here, we analyze the resulting wave emissions by two approaches. First, our linear dispersion analysis shows that several electron Bernstein harmonics can be unstable, their number being proportional to the drift, yet limited by the ion beam temperature. Second, the three local populations (incoming electrons/ions and reflected ions) of the foot region are introduced in full electromagnetic particle-in-cell (PIC) periodic simulations in order to analyze the nonlinear regime of the ECDI. The main results are the following: (1) High gyroharmonics develop over a short time scale less than the lower hybrid period. (2) The spectral power shifts toward lower k modes to accumulate on the first harmonic under the effects of two complementary processes: (i) trapping of the reflected ion beam and (ii) resonance broadening. The latter acts to demagnetize the electrons in the dispersion relation. It initially applies to very high k modes ($k\rho_e >> 1$) and progressively, as time evolves, to lower k modes, invalidating the existence of all gyroharmonics except the first one. (3) In the late stage, a magnetic field component surprisingly develops in the energy spectrum that had so far been electrostatic. (4) The electrons are heated, which represents a source of preheating in the foot region of the shock front.

Citation: Muschietti, L., and B. Lembège (2013), Microturbulence in the electron cyclotron frequency range at perpendicular supercritical shocks, *J. Geophys. Res. Space Physics*, *118*, 2267–2285, doi:10.1002/jgra.50224.

1. Introduction

[2] Supercritical quasi-perpendicular collisionless shocks are commonly observed and often invoked as important sources of particle acceleration and heating. One major difficulty of analysis is that such acceleration/heating takes place via intricate wave-particle interactions over quite different spatial and temporal scales within the shock front region. In supercritical regime, it is well known that part of the incoming ions are reflected at the steepened ramp and accumulate locally to form a foot during their gyromotion before finally penetrating downstream. This accumulation is at the origin of the shock front self-reformation, which is one of the processes responsible for shock front nonstationarity as shown in decades of particle-in-cell (PIC) simulations [*Biskamp and Welter*, 1972; *Lembege and Dawson*, 1987; *Lembege and Savoini*, 1992; *Scholer et al*., 2003; *Hada et al*., 2003; *Chapman et al*., 2005]. Besides the self-reformation that occurs in some parameter regime, reflected ions are also responsible for a chain of processes leading to dissipation and irreversibility, a main ingredient of shock physics. A blowup of the foot region (Figure 1) shows the three different populations that coexist during the gyration of the reflected ions: incoming electrons/ions and reflected ions which can be described by an ion beam during a part of their gyration. These three populations represent a local set of out-of-equilibrium particle distributions and hence are potential sources of wave instabilities excited by the relative drift between the populations. The unstable waves then grow sufficiently to alter these distributions while reducing the free energy, which results in irreversible dissipation.

[3] Several works have already examined various instabilities which are expected within the shock front and are summarized in the review by *Wu et al.* [1984]. In particular, with the help of PIC simulations, recent studies have addressed instabilities excited along the shock normal when the angle θ_{BN} between the normal of the shock front and the upstream magnetostatic field is either exactly perpendicular or slightly off 90°. Two types of instabilities have been correspondingly identified: For $\theta_{BN} = 90°$, a variety of the electron cyclotron drift instability caused by the

[1]Space Sciences Laboratory, University of California, Berkeley, California, USA.
[2]Latmos-CNRS, Université de Versailles-Saint-Quentin, Guyancourt, France.

Corresponding author: L. Muschietti, Space Sciences Laboratory, University of California, 7 Gauss Way, Berkeley, CA 94720, USA. (laurent@ssl.berkeley.edu)

2169-9380/13/10.1002/jgra.50224

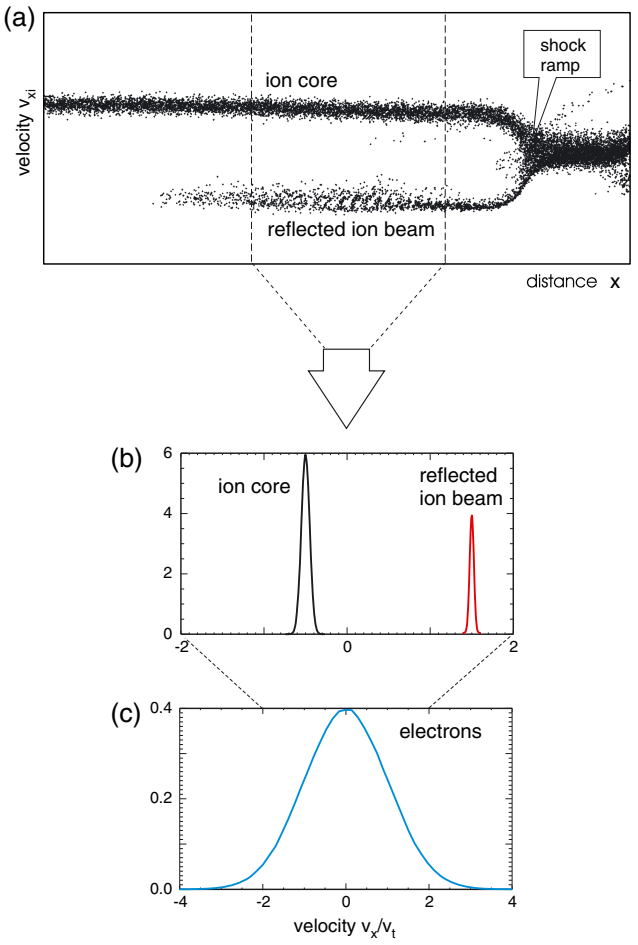

Figure 1. Models of ion and electron populations identified within the foot region of a supercritical perpendicular shock from a 1-D PIC simulation (for typical Alfven Mach M_A= 3–5); (a) view of the ion phase space; (b and c) blowup of the local ion core, reflected ion beam, and electron distributions to be introduced in the linear dispersion analysis (section 2) and the 1-D periodic simulation (sections 3 and 4). The whole study is performed in the electron rest frame. Note that the drift of each population is such that total current is zero (as expected in the foot region).

reflected ion beam and the electrons (so-called ECDI herein) [*Muschietti and Lembege*, 2006] and for $\theta_{BN} \neq 90°$, the modified two-stream instability (so-called MTSI herein) [*Scholer et al.*, 2003; *Matsukiyo and Scholer*, 2003]. In addition, for very high Mach numbers in astrophysical context such as supernova remnants where the relative drift between reflected ions and the electron population is very large, the Buneman instability plays an important role [*Shimada and Hoshino*, 2000].

[4] The present study, which is devoted to the role of waves in the electron cyclotron frequency range, will focus on the ECDI excited within the foot region. It represents an extension of a previous work [*Muschietti and Lembege*, 2006]. Unlike in that work, however, here the three populations are introduced separately and correspond to models of typical local distributions encountered within the foot region of a supercritical shock (with M_A around 3–5, as in Figure 1). This allows us to zoom in on the foot region and in an area of order 20 electron inertia length to study the evolution of the ECDI in detail. Results of linear dispersion analysis are summarized in section 2. Numerical PIC simulation conditions are summarized in section 3, while corresponding numerical results are presented in sections 4 and 5. The comparison with the ion-acoustic instability (so-called IAI herein) deserves a particular interest and is presented in section 6. Discussion and comparison of present results with previous works is deferred to section 7. Lastly, section 8 summarizes our conclusions.

2. Study of Dispersion Properties

[5] We suppose that the standard assumptions of an infinite, uniform plasma apply to the flat portion of the magnetic foot and adopt a coordinate system in which the electrons are at rest while ion beam and ion core drift in opposite x-directions in a way such that the net current is zero (as expected within the foot region). Key elements of the dispersion tensor Q are given explicitly below.

[6] The electrons are taken as hot and magnetized. They have a thermal velocity $v_{te} = \sqrt{T_e/m}$ and a gyroradius $\rho_e = v_{te}/\Omega_{ce}$, where Ω_{ce} denotes their cyclotron frequency. In their contribution to the susceptibility, one can recognize the term for electron cyclotron Bernstein waves,

$$Q_{xx,e} = -\frac{1}{k^2\lambda_{de}^2}\left[-1 + \Lambda_0(\eta) + 2\sum_{n=1}^{\infty}\Lambda_n(\eta)\frac{\omega^2}{\omega^2 - n^2\Omega_{ce}^2}\right]. \quad (1)$$

Here $\Lambda_n(\eta) \equiv I_n(\eta)\exp(-\eta)$ is the modified Bessel function which has for argument $\eta \equiv (k\rho_e)^2 = (\omega_{pe}/\Omega_{ce})^2(k\lambda_{de})^2$ with the plasma frequency ω_{pe} and the Debye length λ_{de}.

[7] Ions are taken as unmagnetized, which is justified on the time scale considered. The ion beam has density $\alpha < 0.5$, thermal spread v_{tb}, and drift V_b, while the ion core has, respectively, $1-\alpha$, v_{tc}, and $-V_c$, where $V_c = V_b\,\alpha/(1-\alpha)$. Their contribution to the susceptibility reads as

$$Q_{xx,i} = -\frac{\alpha}{k^2\lambda_{de}^2}\frac{T_e}{2T_b}Z'\left(\frac{\omega - kV_b}{\sqrt{2}kv_{tb}}\right) - \frac{1-\alpha}{k^2\lambda_{de}^2}\frac{T_e}{2T_c}Z'\left(\frac{\omega + kV_c}{\sqrt{2}kv_{tc}}\right), \quad (2)$$

with Z the usual plasma dispersion function [*Fried and Conte*, 1961].

[8] For the perpendicular geometry considered here, where $\mathbf{B_0}$ points in the $\hat{\mathbf{z}}$-direction and the wave vector $\mathbf{k}$ in the $\hat{\mathbf{x}}$-direction, the electrostatic dispersion relation is simply

$$1 + Q_{xx,e} + Q_{xx,i} = 0. \quad (3)$$

The instability is due to a coupling between electron cyclotron Bernstein modes and ion beam modes. Figure 2a shows 14 Bernstein harmonics in a frequency-versus-wave number plot. The successive branches have the characteristic negative group velocity up to the upper hybrid branch, which is here marked in blue. The frequency of the n branch lies between $n\Omega_{ce}$ and $(n+1)\Omega_{ce}$ and tends to $n\Omega_{ce}$ at high $k\rho_e$. Superimposed in red is the Doppler frequency of the beam $\omega = kV_b$. Close to each intersection between the Bernstein modes and the red line, an instability is possible. Results from numerically solving the electrostatic dispersion relation (3) are displayed in Figures 2b and 2c, where we used the plasma parameters summarized in Table 1 for the three populations. Each Bernstein branch reconnects with

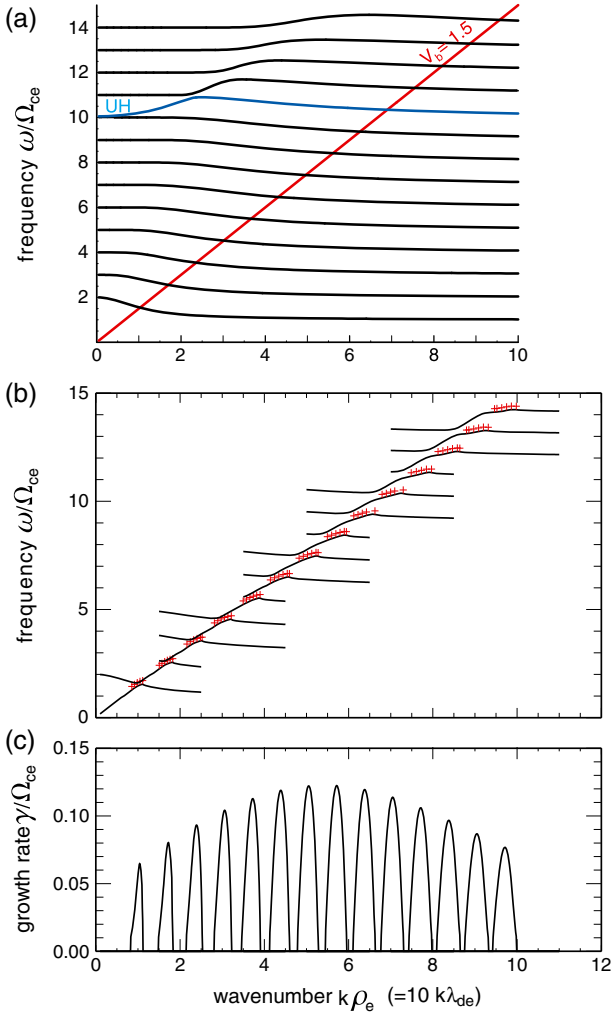

Figure 2. Linear dispersion analysis of the ECDI for the reference case herein: $V_b/v_{te} = 1.5$, $\omega_{pe}/\Omega_{ce} = 10$, $T_b/T_e = 0.25$ and ion beam density $\alpha = 0.25$. (a) Schematic where ion beam curve and electron Bernstein curves are superimposed: the ion beam mode (in red) intersects the 14 first branches of electron Bernstein modes (in black), raising the possibility of coupling (both below and above the upper hybrid branch shown in blue). (b) Numerical solution of equation (3) showing the coupling of the Bernstein waves with the ion beam mode (frequency's real part) and the associated unstable ranges marked by red crosses "+." (c) Growth rate (frequency's imaginary part) defined at the location of the red crosses (in Figure 2b) corresponding to the 14 branches. The plasma parameters used are defined in Table 1.

part of the ion beam mode. An unstable imaginary part develops over a narrow range of wave numbers whose location is marked here by small red crosses. Thus, the emission is expected to occur in discrete bands of frequency as well as wave number. Figure 2c shows the actual growth rate for each band as a function of wave number. Note how the envelope to the individual growth rates display a "knee" shape whereby harmonics *6–9* have maximum growth as compared with lower and higher harmonics. We shall see below the reason for that feature. As for the physical reason behind the unusual coupling of ion and electron frequencies, it lies in the short wavelengths and a substantial value of the drift. Each electron frequency at multiples of Ω_{ce} is Doppler-shifted by kV_b and, seen from the beam, appears in the range of ion-acoustic frequencies to which the ion beam can respond.

[9] Returning to the discreteness of the emissions, we stress that it is a signature of this instability and point out the following. For low harmonics, the unstable portion of the dispersion curve has a slope $|d\omega/dk|$ close to the beam drift (see locations of crosses in Figure 2b). For high harmonic branches, the unstable portion of the dispersion curve becomes flatter. Thus, the unstable bandwidth δk associated to each harmonic increases for higher harmonics. Conversely, the bandwidth expressed in $\delta\omega$ narrows. As will be seen in section 2.2, the feature is related to the finite temperature of the beam.

[10] In order to understand the impact of thermal effects, we first discuss the case of a cold and slow ion beam, for which an analytical solution can be found [*Wong*, 1970; *Lampe et al.*, 1972], and then compare it to numerical solutions of the dispersion relation including ion thermal effects.

2.1. Cold Ions and Small Drift: Analytical Approach

[11] After lengthy analytical manipulations which are detailed in the work of *Lampe et al.* [1972, see Appendix A] the electron susceptibility in the limit $k\rho_e > 1$ can be rewritten from the familiar form (1) to the less usual expression

$$Q_{xx,e} = \frac{1}{(k\lambda_{de})^2}\left\{1 - \sqrt{\pi}\zeta e^{-\zeta^2}\left[\cot\left(\frac{\omega}{\Omega_{ce}}\pi\right) - i\,\mathrm{erf}(i\zeta)\right]\right\}, \quad (4)$$

where ζ is the normalized phase velocity, $\zeta \equiv \omega/(\sqrt{2}kv_{te})$. As for the ions, their susceptibility in the cold limit takes the simple form

$$Q_{xx,i} = -\frac{\alpha\,\omega_{pi}^2}{(\omega - kV_b)^2} - \frac{(1-\alpha)\omega_{pi}^2}{(\omega + kV_c)^2}, \quad (5)$$

with ω_{pi} the ion plasma frequency. Since we know from the discussion of Figure 2 that an unstable root has $\omega_r \sim kV_b \gtrsim n\Omega_{ce}$, the second term in (5), which is due to the ion core, is expected to be of order $(1-\alpha)^3(m/M)(\omega_{pe}/n\Omega_{ce})^2 \ll 1$ and

Table 1. Species Characteristics in Normalized Units

	Electrons	Ion Core	Ion Beam
Density	$n_e = 1.0$	$n_c = 0.75$	$n_b = 0.25$
Gyrofrequency	$\Omega_{ce} = 1.$	$\Omega_{cc} = 2.5 \times 10^{-3}$	$\Omega_{cb} = 2.5 \times 10^{-3}$
Plasma frequency	$\omega_{pe} = 10.$	$\omega_{pc} = 0.433$	$\omega_{pb} = 0.25$
Gyroradius	$\rho_e = 1.$	$\rho_c = 20.$	$\rho_b = 10.$
Debye length	$\lambda_{de} = 0.1$	$\lambda_{dc} = 0.115$	$\lambda_{db} = 0.1$
Temperature	$T_e = 1.$	$T_c = 1.$	$T_b = 0.25$
Thermal velocity	$v_{te} = 1.$	$v_{tc} = 5. \times 10^{-2}$	$v_{tb} = 2.5 \times 10^{-2}$
Kinetic/magnetic energy	$\beta_e = 0.08$	$\beta_c = 0.06$	$\beta_b = 0.005$

can be neglected. The dispersion relation (3) can therefore be written as

$$1 + k^2\lambda_{de}^2 - \alpha\frac{(k\lambda_{de}\,\omega_{pi})^2}{(\omega - kV_b)^2} = \sqrt{\pi}\zeta e^{-\xi^2}\left[\cot\left(\frac{\omega}{\Omega_{ce}}\pi\right) - i\,\mathrm{erf}(i\zeta)\right]. \quad (6)$$

On the left-hand-side of equation (6), one recognizes the acoustic beam mode

$$\omega_r - kV_b = -\frac{kc_s\alpha^{1/2}}{(1 + k^2\lambda_{de}^2)^{1/2}}, \quad (7)$$

where $c_s = (T_e/M)^{1/2}$ is the acoustic speed. The role of the cotangent on the right-hand side is to select in the broad acoustic spectrum frequencies that are periodically spaced as harmonics of the cyclotron frequency.

[12] Let us now assume that the drift is small compared to the electron thermal speed, $V_b < v_{te}$. Return to the top panel of Figure 2 and consider a diagonal with a lesser slope than the red line drawn. The Doppler frequency of the beam $\omega = kV_b$ would now intersect the Bernstein branches at high $k\rho_e$, where the frequency of branch n is actually close to $n\Omega_{ce}$. Furthermore, the normalized phase velocity is below unity, i.e., $\zeta < 1$. Therefore, in the square bracket of (6), one can neglect the erf term as compared with the cotangent term, and in front of the bracket one can replace the exponential term by unity. If we write $\omega = n\Omega_{ce} + i\gamma_n$ with $|\gamma_n| << |n\Omega_{ce} - kV_b|$, we find the growth of each harmonic to be

$$\gamma_n = \Omega_{ce}\left(\frac{\alpha}{8\pi}\frac{m}{M}\right)^{1/4}\frac{n^{1/2}}{\left(1 + k^2\lambda_{de}^2\right)^{3/4}}. \quad (8)$$

The expression is essentially the same as in *Wong* [1970] except for the factor α (beam density over total ion density). One remarks that as long as $k\lambda_{de} << 1$, the value of γ_n increases as $n^{1/2}$. The first gyroharmonic has therefore the slowest growth. Yet, since n and k grow in proportion via $kV_b \approx n\,\Omega_{ce}$, the growth γ_n reaches a maximum for some integer n_0 and then decreases slowly. The value of n_0 is given by

$$n_0 = int[(V_b/v_{te})(\omega_{pe}/\Omega_{ce})/\sqrt{2}]. \quad (9)$$

Hence, one can conclude that the number of gyroharmonics excited is directly proportional to the drift. In contrast, the number of harmonics is inversely proportional to the magnetization of the plasma, Ω_{ce}/ω_{pe}. Be aware, however, that equation (9) does not include ion thermal effects that can significantly reduce it, as discussed in section 2.2.

2.2. Warm Ions: Numerical Analysis

[13] For beam drifts other than small, the transcendental functions in the right-hand side of equation (6) cannot be expanded, and no algebraic solution can be found. In addition, equation (6) does not include thermal effects of the ions. We thus return to equation (3) with susceptibilities (1) and (2) and have recourse to numerical solutions.

[14] Figure 3 shows the effects of beam pressure and Landau damping on the growth rate. We use three beam temperatures (T_b/T_e = 0.1, 0.25, and 1.0) and display the resulting modified growth in the successive harmonic bands. The horizontal axis is plotted here in terms of $k\lambda_{de}$ instead of $k\rho_e$ in order to emphasize the strong effect of T_b where the wave number $k\lambda_{de}$ approaches unity. The stars indicate the

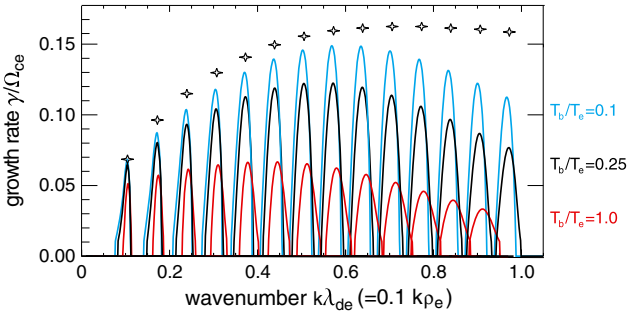

Figure 3. Similar to Figure 2c, growth rates of the ECDI (numerical solution of equation (3)) for three different ion beam temperatures. All other plasma parameters (see Table 1) are identical to those of Figure 2. The stars * report the maximum growth rates defined by the fluid formula for a cold beam (equation (8)).

maximum growth for each harmonic according to the fluid formula γ_n (equation (8)). Although formula (8) does not strictly apply to a beam drift $V_b/v_{te} = 1.5$ as considered here, we can see that it provides a fairly good proxy for the cold beam case with $T_b/T_e = 0.1$. This is specially true for lower harmonics such that $k\lambda_{de} < 0.5$. For higher wave numbers and harmonics, the increasing beam pressure degrades the growth rate. The instability tends to change character from "reactive" to "resistive" [*Dum*, 1989]. We recall that a "reactive" instability depends on fluid parameters describing the beam-plasma system. Thus, equation (8) characterizes the beam through its density only. On the other hand, a "resistive" instability depends on a small number of resonant particles that provide negative Landau damping. In the latter case, the real part of the frequency remains close to that of the plasma eigenmode, while the imaginary part is related to the slope of the distribution function at the phase velocity. In Figure 3, the reactive growth rate (indicated by the stars) is strongly degraded for high wave numbers. This is due to thermal effects (increased pressure and increased Landau damping), which augment with k and T_b. The general effect is to shift the maximum growth toward gyroharmonics well below the integer value n_0 defined in equation (9). Confirming the transition from reactive toward a weaker, resistive type of instability, the frequency bandwidth $\delta\omega$ for each harmonic (not shown) diminishes, and the frequencies approach the Bernstein mode values, i.e., the eigenmode values.

[15] At last, we stress that the information obtained in this linear analysis is helpful for designing simulations of such an instability. The simulation box needs to have a length L sufficient to accommodate long wavelengths at the first harmonic such as $\lambda = 60\lambda_{de}$ and to yield $\Delta k = 2\pi/L$ small enough to resolve the narrow emission bands. Simultaneously, the grid cells themselves need to be sufficiently small to resolve features on the Debye scale.

3. Simulation Conditions

[16] Present simulations allow a very detailed analysis (over an enlarged spatial scale) of the instabilities developing in the foot region of a supercritical shock in the presence of the three particle components illustrated in Figures 1b

and 1c. We use a periodic 1-D full PIC code where both electrons and ions are described as an assembly of individual particles. Detaching the present simulations from a full shock simulation enables us to analyze such instabilities with high time and spatial resolution during a time range that remains small as compared to the shock dynamics scale; one can carefully analyze rapid instabilities developing over a time scale much shorter than the self-reformation cyclic period (itself comparable to the ion gyroperiod). Following this route allows one to access waves with high frequency (here several electron gyroharmonics) and with a spatial scale of a few Debye lengths, which develop simultaneously with the large-scale ion dynamics.

[17] Among the many simulations of ECDI performed for our study, we report herein on one specific simulation (used as a reference) with a grid that covers 1024 cells and spans 1024 Debye lengths (or equivalently 102.4 electron gyroradii or 20.5 electron inertia lengths). The resulting wave number resolution is $\Delta k = 6 \times 10^{-3} \lambda_{de}^{-1}$, which allows to "hit" the growth range of each gyroharmonics, including the first harmonic with its narrow δk (see Figure 2c). The electric and magnetic fields have five self-consistent components: E_x, E_y, E_z, and B_y, B_z among which only E_x is electrostatic (solution of Poisson equation), while the others are purely electromagnetic (solutions of full Maxwell equations). As a reminder, the unique direction $\hat{\mathbf{x}}$, which lies in the coplanarity plane defined by the background magnetic field $\mathbf{B}_o$ and the shock normal $\mathbf{n}$, is perpendicular to $\mathbf{B}_o$ such that $\hat{\mathbf{x}} \cdot n \sim 1$. In our previous work that simulated a full shock [*Muschietti and Lembege*, 2006], the direction $\hat{\mathbf{x}}$ corresponded to that of the normal to the shock front.

[18] The particles have three velocity components, v_x, v_y, and v_z, and are represented by 409,600 macroparticles for each plasma component, namely, 400 electrons, 400 core ions, and 400 beam ions per cell. The PIC code has been tailored to keep the same number of macroparticles for each population while one parameter allows to vary the relative percentage of ion beam density to core density. The simulation is performed in the electron frame; then, core and beam ions undergo opposite drifts in proportion to their relative density so that the total current is zero (as expected in the foot region of a shock). All quantities are in computer units, which is indicated by a tilde "~", and are normalized (as in previous simulations [see *Lembege and Dawson*, 1987]) as follows. The spatial coordinate is $\tilde{x} = x/\Delta$, velocity $\tilde{v} = v/\omega_{pe}\Delta$, time $\tilde{t} = \omega_{pe}t$, electric field $\tilde{E} = eE/m\omega_{pe}^2\Delta$, and magnetic field $\tilde{B} = eB/m\omega_{pe}^2\Delta$. The parameters Δ, ω_{pe}, m, and e are, respectively, the numerical grid size, the electron plasma frequency, the electron mass, and the electric charge. All basic parameters are summarized as follows: velocity of light $\tilde{c} = 50$, mass ratio of proton versus electron $M/m = 400$, and ambient magnetic field $|\tilde{B}_o| = 5$, which yields a ratio $\tilde{\omega}_{pe}/\tilde{\Omega}_{ce} = 10$. The lower hybrid frequency is $\tilde{\omega}_{lh} = 5 \times 10^{-3}$ (the lower hybrid period being $\tilde{\tau}_{lh} = 1256$), the Alfven velocity is $\tilde{V}_A = 0.25$, and the relative density of the ion beam is $\alpha = N_b/(N_b + N_c) = N_b/N_e = 0.25$. Initially, electrons and core ions have the same temperature, $T_e = T_c = 1$, while the ion beam is a little cooler, $T_b = 0.25$. The foot plasma parameters expressed in computer units are summarized in Table 2 for each particle population.

Table 2. Species Characteristics in Simulation Units

Description	Parameter	Electrons	Ion Core	Ion Beam
Gyrofrequency	$\tilde{\Omega}_c$	0.1	2.5×10^{-4}	2.5×10^{-4}
Plasma frequency	$\tilde{\omega}_p$	1.	4.33×10^{-2}	0.025
Gyroradius	$\tilde{\rho}$	10.	200.	100.
Debye length	$\tilde{\lambda}_d$	1.	1.15	1.
Inertia length	$\tilde{c}/\tilde{\omega}_p$	50.	1.15×10^3	$2. \times 10^3$
Thermal velocity	$\tilde{v}_t$	1.	$5. \times 10^{-2}$	2.5×10^{-2}
Kinetic/magnetic energy	β	0.08	0.06	0.005

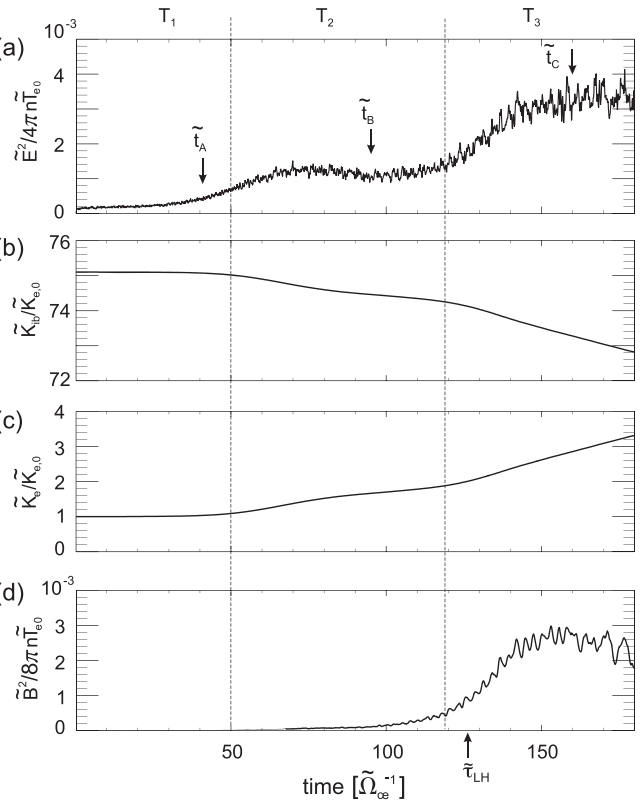

Figure 4. PIC simulation with plasma parameters of Table 2. Time histories of (a) the electrostatic field energy, (b) the ion beam kinetic energy, (c) the electron kinetic energy, and (d) the magnetic field energy. For comparison's sake all dimensionless energies are normalized in the same way by $\tilde{K}_{eo}$, the electron kinetic energy at time $\tilde{t} = 0$. The time range is divided into three stages T_1, T_2, and T_3 and covers 1.43 $\tilde{\tau}_{LH}$ (with $\tilde{\tau}_{LH}$ the lower hybrid period). Selected snapshot times $\tilde{t}_A = 41$, $\tilde{t}_B = 95$, and $\tilde{t}_C = 160\,\tilde{\Omega}_{ce}^{-1}$ will be referred to in the following figures.

4. Simulation Results

[19] Figure 4 shows an overview of the simulation run. The history of four global energy quantities is displayed over a time span of 1.43 $\tilde{\tau}_{lh}$, where $\tilde{\tau}_{lh}$ is the lower hybrid period. In the graph of the electrostatic energy (Figure 4a), one can identify three stages, which have been delimited by vertical, dashed lines and denoted, respectively, T_1, T_2, and T_3. During the early stage T_1, which we consider as

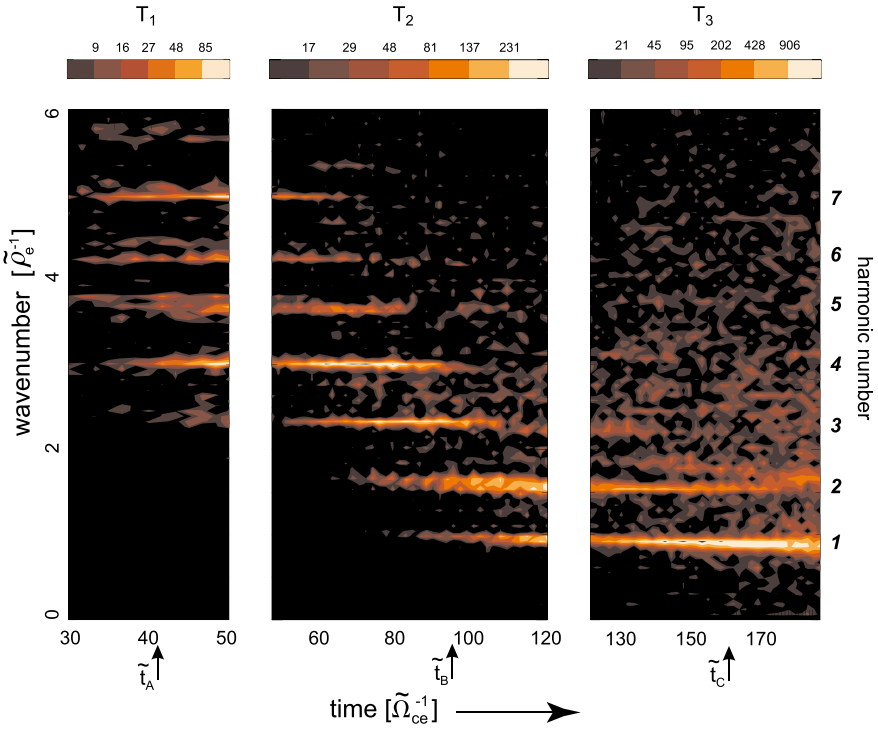

Figure 5. Evolution of the electrostatic energy spectrum during the PIC simulation. Three separate panels (with changing scale as indicated in color bars above) show the harmonics excited during the successive stages T_1, T_2, and T_3. Italicized figures on the right-hand side label the Bernstein harmonics. Selected snapshot times $\tilde{t}_A$, $\tilde{t}_B$, and $\tilde{t}_C$ of Figure 4 are marked with arrows.

corresponding to the linear regime, several high-frequency harmonics with fast growth rates are excited, as will be discussed in relation with Figure 5. During stage T_2 (first nonlinear stage), the electrostatic energy appears to saturate. We shall see that this saturation corresponds to a redistribution of the spectral energy toward lower harmonics. Finally, the electrostatic energy rises again during stage T_3 (second nonlinear stage) when it augments threefold. The kinetic energy of the ion beam $\tilde{K}_{ib}$ (Figure 4b) indicates that the beam loses a few percent of its energy, feeding the instability. Meanwhile, most of the energy lost by the beam reappears in the kinetic energy of the electrons $\tilde{K}_e$ (Figure 4c), which increases threefold in the course of the run. We point out that all the quantities displayed in Figure 4 have been normalized in the same way by the initial kinetic energy of the electrons $\tilde{K}_{e,0} \equiv n\tilde{T}_{e,0}$. It is thus evident that at any given time the energy in the waves is a very small fraction of the energy being transferred from the ions to the electrons. The wave turbulence acts as a "conduit" between the ion beam and the electrons. Lastly, Figure 4d displays the magnetic energy, which indicates that the late nonlinear stage (T_3) comprises an unexpected and significant magnetic component.

[20] Let us now examine the temporal evolution of the electrostatic spectrum $|\tilde{E}_k|^2$ shown in Figure 5. The three panels replicate the stages T_1, T_2, and T_3 introduced in Figure 4. Be aware that the scale of $|\tilde{E}_k|^2$, which is indicated with color bars at the top, changes between panels in order to follow the evolution in spectral intensity. The italicized figures located on the right-hand side label the Bernstein harmonics. So, one can see that near the end of stage T_1, harmonics *7*, *6*, *5*, and *4* are excited in agreement with their rapid linear growth rates. We note that harmonic *8* is barely visible and harmonics *9*, *10*, and *11* not at all in the simulation despite their equally fast linear growth rates. As we shall see later in section 5.1, the growth of waves at these large wave numbers is inhibited by resonance broadening. During stage T_2, the excited harmonics die out, while harmonics *3*, *2*, and *1* grow and appear more clearly. Finally, during stage T_3, the spectral energy concentrates on the first harmonic, while harmonics *3* and *2* (and higher) fade away. Thus, one observes a shift of the spectrum from high wave number harmonics to lower harmonics, or from high frequency to low frequency, in what may look like an inverse cascade which ends up on the first harmonic. Below, in section 5, we will analyze the reasons behind this striking behavior. Meanwhile, we discuss the phase space of the ion beam, which also reflects the evolutionary shift from shorter to longer wavelengths.

4.1. Ion Beam

[21] We have chosen three times representative of the three stages T_1, T_2, and T_3 and have reported them in Figures 4 and 5 as $\tilde{t}_A$, $\tilde{t}_B$, and $\tilde{t}_C$. Figure 6 displays snapshots of the ion beam at these times. Figures 6a, 6b, and 6c show the $[\tilde{x}, \tilde{v}_x]$ phase space over a limited portion of the simulation box that spans $30\tilde{\rho}_e$. At time $\tilde{t} = \tilde{t}_A$, the first signs of trapping become visible in the structuring of phase space within the range $\tilde{v}_x/\tilde{v}_{te} = [1.4, 1.5]$. Note the short wavelength (we measure $\tilde{\lambda} = 1.3\tilde{\rho}_e$) in agreement with the high wave number spectrum present during stage T_1 ($\tilde{t} = \tilde{t}_A$ in left panel of Figure 5, harmonic *7*). It is instructive to define a charac-

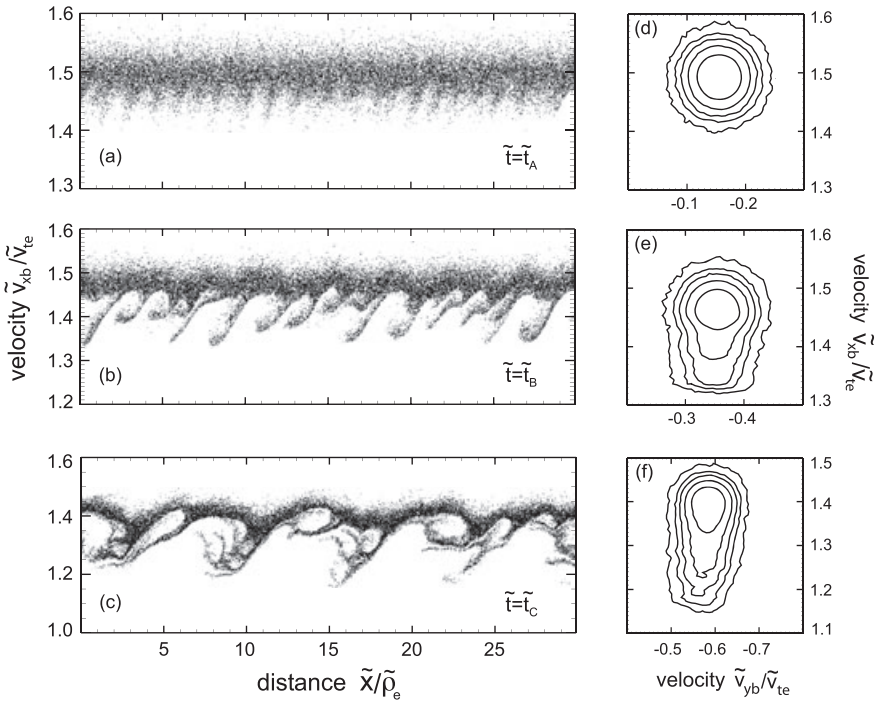

Figure 6. Snapshots of the ion beam at times $\tilde{t}_A$, $\tilde{t}_B$, and $\tilde{t}_C$ of Figures 4 and 5. Panels (a, b, c): Enlarged view of the phase space. Panels (d, e, f): Isocontours distribution function $f(\tilde{v}_y, \tilde{v}_x)$ at the same times. The distributions have been obtained by binning particles from half the simulation box and hence are averaged over many wavelengths. The innermost contour is at $f_{max}/3$ with f_{max} the maximum value of f. Subsequent contours are at $f_{max}/9$, $f_{max}/27$, $f_{max}/81$, and $f_{max}/243$.

teristic nonlinear time that is based on the bounce time of the beam's ions in the wave [e.g., *Nicholson*, 1983, chap. 6]

$$\tilde{\tau}_{nl} \equiv \frac{2\pi}{\tilde{\Omega}_{ce}} \sqrt{\frac{M}{m} \frac{\tilde{\Omega}_{ce}}{\tilde{\omega}_{pe}} \frac{1}{\tilde{k}\tilde{\rho}_e} \frac{1}{\tilde{E}_x}} \tag{10}$$

and to evaluate it in relation to Figure 6. Using values for the wave electric field $\tilde{E}_x$ and wave number $\tilde{k}$ typical of time $\tilde{t}_A$, such as $\tilde{E}_x = 0.05$ and $\tilde{k}\tilde{\rho}_e = 5$, one obtains $\tilde{\tau}_{nl} = 79\tilde{\Omega}_{ce}^{-1}$. By $\tilde{t} = \tilde{t}_A$, the mode $\tilde{k}\tilde{\rho}_e = 5$ has been intense since $\tilde{t} = 30$, i.e., for a duration of only $10\Omega_{ce}^{-1}$ (see left panel of Figure 5), hence to observe just early signs of trapping in some ions seems consistent. Later, at time $\tilde{t} = \tilde{t}_B$ (Figure 6b), the trapping is more pronounced, and longer wavelengths appear to structure the ion phase space. Although several wavelengths are clearly involved, we estimate the dominant one to be $2.7\tilde{\rho}_e$, in agreement with harmonic *3* of the spectrum displayed in the middle panel of Figure 5. We can again evaluate $\tilde{\tau}_{nl}$ using values typical of time $\tilde{t} = \tilde{t}_B$ such as $\tilde{E}_x = 0.1$ and $\tilde{k}\tilde{\rho}_e = 2.3$. One obtains $\tilde{\tau}_{nl} = 83\tilde{\Omega}_{ce}^{-1}$. Since harmonic *3* has been intense for a duration $40\tilde{\Omega}_{ce}^{-1}$ by $t = t_B$ (see middle panel of Figure 5), one can expect half a trapping loop as observed. Finally, at time $\tilde{t} = \tilde{t}_C$ (Figure 6c), the ion phase space evidences a strong signature of trapping in the long-wavelength mode of the first harmonic at $k\tilde{\rho}_e = 1$. Structures of shorter scale, remnants of the interaction of the ions with the higher harmonics, are carried away in the trapping associated with the first harmonic. This causes a loss of coherence in the high harmonics and hence their disappearance from the spectrum. The effect will be discussed in detail in section 5.

[22] The distribution function of the ion beam $f(\tilde{v}_y, \tilde{v}_x)$ at times $\tilde{t}_A$, $\tilde{t}_B$, and $\tilde{t}_C$ is shown in Figures 6d, 6e, and 6f by means of contours and shows three main features. First, all the "tongues" in phase space, when averaged over many wavelengths, add up and form a tail to the ion beam roughly at a 10% level from the beam's top. Second, since the ions are magnetized in the simulation (unlike in our dispersion study), the beam slowly gyrates during the course of the run at the rate $\tilde{\Omega}_{ci} = \tilde{\Omega}_{ce}/400$. Be aware of the changing scales on the axes between Figures 6d, 6e, and 6f, and note how the center of the innermost contour shifts from one snapshot to the next. As expected, the shift obeys $\tilde{v}_x \sim \cos(\tilde{\Omega}_{ci}t)$ and $\tilde{v}_y \sim -\sin(\tilde{\Omega}_{ci}t)$. Third, the drift of the beam as computed by integrating over all beam particles decreases in time due to the tail formation and the loss of kinetic energy feeding the instability.

4.2. Direct Measurement of the Wave Frequencies

[23] So far we have simply assumed that the unstable waves observed in the simulation had the frequencies associated to their wave number by the dispersion relation presented in section 2. It seems desirable, though, to independently determine these frequencies. To this end, several "probes" were set up at various, fixed positions in the box and recorded the local electric and magnetic field components versus time. Records of the electrostatic field $\tilde{E}_x$ and

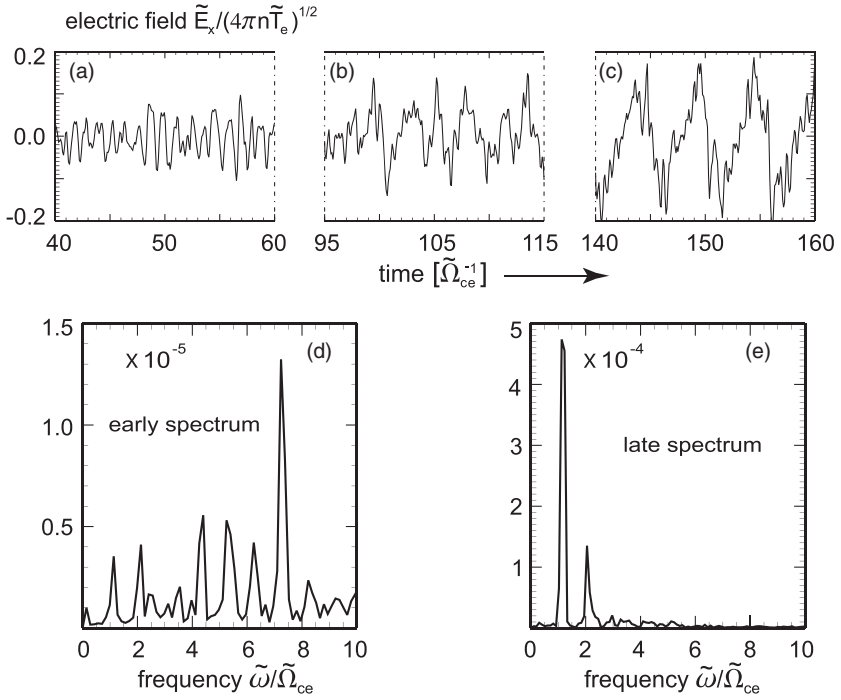

Figure 7. Record of the electrostatic signal $\tilde{E}_x$ in three successive time ranges (a) $\tilde{\Omega}_{ce}\Delta\tilde{t}$ = [40 – 60], (b) $\tilde{\Omega}_{ce}\Delta\tilde{t}$ = [95 – 115], and (c) $\tilde{\Omega}_{ce}\Delta\tilde{t}$ = [140 – 160]. Corresponding power spectra computed within (d) early time range $\tilde{\Omega}_{ce}\Delta\tilde{t}$ = [40 – 60] and (e) late time range $\tilde{\Omega}_{ce}\Delta\tilde{t}$ = [140 – 160]. Note the change in scale between Figures 7d and 7e.

of the magnetic field $\tilde{B}_z$ are shown in Figures 7 and 8, respectively. Within each figure, the records of $\tilde{E}_x$ and $\tilde{B}_z$ have been sequenced in three successive time ranges each lasting $20\tilde{\Omega}_{ce}^{-1}$ so as to render details visible. The first time range $\tilde{\Omega}_{ce}\tilde{t}$ = [40, 60] (Figure 7a) illustrates the traces at early time, and $\tilde{E}_x$ clearly shows short-period oscillations.

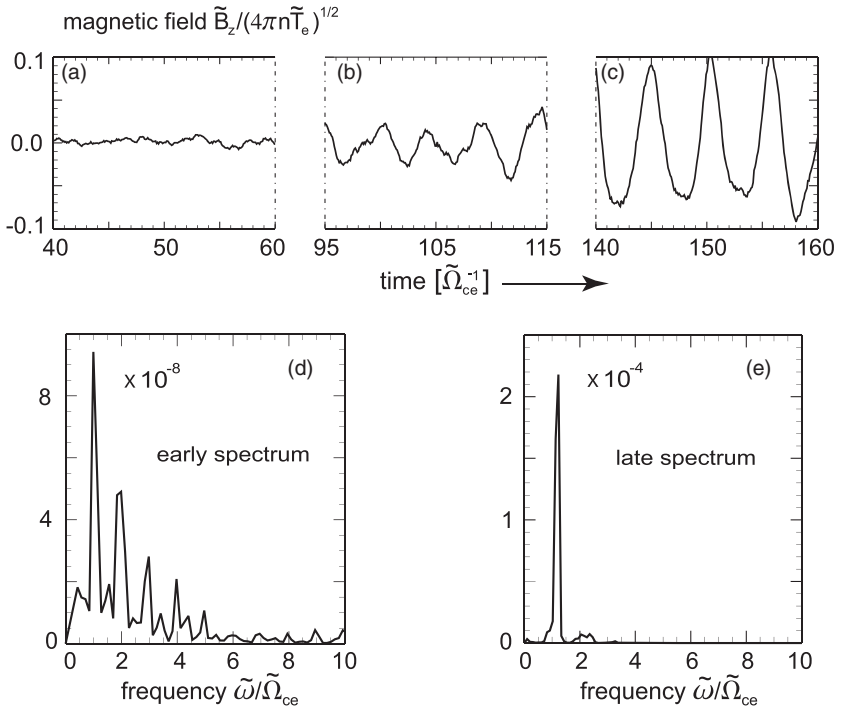

Figure 8. Record of the magnetic signal $\tilde{B}_z$ in the same time ranges as in Figure 7. Corresponding power spectra computed within early time range $\tilde{\Omega}_{ce}\Delta\tilde{t}$ = [40 – 60] and late time range $\tilde{\Omega}_{ce}\Delta\tilde{t}$ = [140 – 160] are displayed in Figures 8d and 8e. Note the change in scale between Figures 8d and 8e.

Its power spectrum (Figure 7d) exhibits several discrete harmonics as expected. In contrast, the trace of $\tilde{B}_z$ (Figure 8a) is weak at this time, even though, surprisingly, its power spectrum (Figure 8d) already reflects some harmonic structure. The first harmonic is especially prominent. In Appendix A, we show that the cross-field conductivity is a rapidly decreasing function of the harmonics, which explains that the spectrum of $\tilde{B}_z$ imperfectly reflects the spectrum of $\tilde{E}_x$. The traces of $\tilde{E}_x$ and $\tilde{B}_z$ in the second range, $\tilde{\Omega}_{ce}\tilde{t} = [95, 115]$, show the emergence of a long-period oscillation close to the electron cyclotron period (Figures 7b and 8b). Finally, the third range, $\tilde{\Omega}_{ce}\tilde{t} = [140, 160]$, illustrates the traces at late time when nearly all the wave power is accumulated on the first harmonic (Figures 7c and 8c). Two remarks are in order regarding the late power spectra of $\tilde{E}_x$ (Figure 7e) and $\tilde{B}_z$ (Figure 8e). First, the frequency of the wave is a little above $\tilde{\Omega}_{ce}$, more precisely, $\tilde{\omega} = 1.3\tilde{\Omega}_{ce}$. Second, the magnetic energy reaches a level comparable to the electric energy, confirming what was already noted about Figure 4. This magnetic buildup raises the question of what oscillating current develops as source to the oscillating $\tilde{B}_z$. One needs to analyze the behavior of the electrons, in particular the deformation of their trajectories during the late stage of the ECD instability. This is done in section 4.3.

4.3. Electrons and Magnetic Signature of the Waves

[24] In a cross-field geometry where $\mathbf{B_o} = (0, 0, B_o)$ and $\mathbf{E} = (E_x, 0, 0)$, it is well known that the response of electrons to an electric field E_x oscillating with frequency ω depends upon the relation of their cyclotron frequency Ω_{ce} to ω. For $\Omega_{ce} \ll \omega$, the electrons oscillate mainly in the $\hat{x}$ direction, whereas for $\Omega_{ce} \gg \omega$, they oscillate mainly in the $\hat{y}$ direction, i.e., perpendicularly to both $\mathbf{B_o}$ and $\mathbf{E}$. What about in a situation where $\omega \sim \Omega_{ce}$ as we have herein during stage T_3 (Figure 7e)? A formal answer is provided by examining the cross-field conductivity σ_{yx} associated to the dispersion tensor, which yields the current j_y caused by a nominal electric field E_x according to linear analysis. In Appendix A, we evaluate σ_{yx} and show that it is a sharply decreasing function of the gyroharmonics. Thus, for high cyclotron harmonics (i.e., $\omega \gg \Omega_{ce}$), the response in the $\hat{y}$ direction is very weak. For the first cyclotron harmonic, though, the response is strong, meaning that the electrons' motion comprises a significant component in the $\hat{y}$ direction. This is the source of a current j_y that generates an oscillating magnetic component B_z in addition to the background field $(0, 0, B_0)$.

[25] There is another approach to understanding the magnetic signature exhibited during the late stage T_3. One may directly examine the behavior of electrons in a given Bernstein wave with frequency $\omega = 1.3\Omega_{ce}$ as determined in Figure 7e. The analysis is detailed in Appendix B, which yields two main points. First, some electrons from the core can be significantly energized and reach speeds on the order of $4v_{te}$ for the wave characteristics we observe during stage T_3. Second, their orbits in (x, v_y) hint to a "striation" of the $[x, v_y]$ phase space (see the example of slanted orbit shown in Figure B1, panel (c)). Now, a striated phase space is indeed evidenced in Figure 9a, which is an enlarged view taken from the simulation at time $\tilde{t} = \tilde{t}_C$ and displays a snapshot of the electrons. Note the slanted, elongated patterns

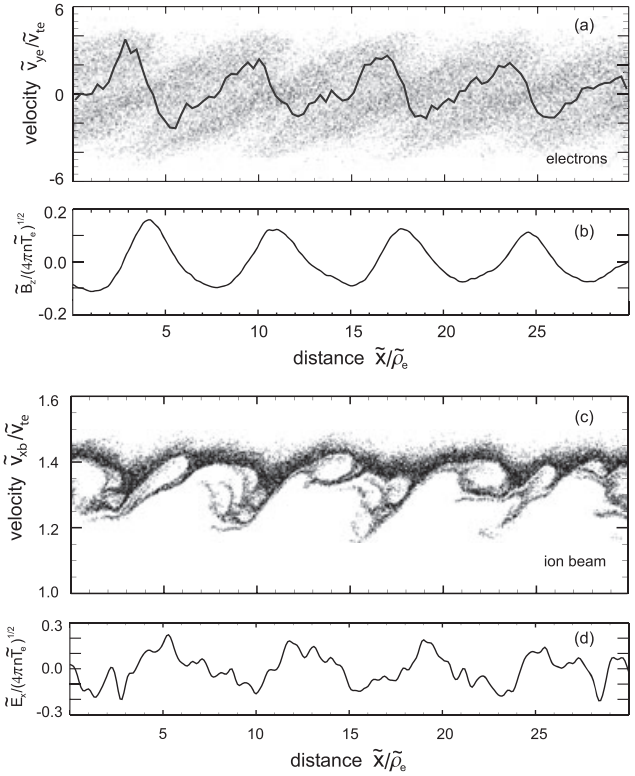

Figure 9. Snapshot at $\tilde{t} = \tilde{t}_C$ combining particle phase space and field information. (a) Enlarged view of the electron phase space $[\tilde{x}, \tilde{v}_{ye}]$ with a thick line indicating the current component $\tilde{J}_{ye}$ obtained by integrating the electrons. (b) Associated spatial profile of the main magnetic field component $\tilde{B}_z$. Corresponding plots (c) of the ion beam phase space and (d) of the electrostatic field $\tilde{E}_x$.

that extend in $\tilde{x}$ over $14\tilde{\rho}_e$. A solid line indicates the corresponding spatial profile of $\tilde{j}_{ye}$. For comparison, we show the spatial profile of $\tilde{B}_z$ in Figure 9b. The phase relation between the two profiles $\tilde{j}_{ye}$ and $\tilde{B}_z$, which are shifted by $\pi/2$, is clearly what can be expected from Ampere's law, $\partial_x B_z = -j_y$. Now, which electrons contribute the most to this current $-\tilde{j}_y$? To answer the question, we have varied the bounds of integration of the first moment $\int \tilde{v}_y f\,(\tilde{x}, \tilde{v}_y)\ d\tilde{v}_y$. It turns out that the main carriers of the current are electrons with speeds $2 < |\tilde{v}_y| < 4$, confirming thus the importance of the accelerated electrons.

[26] Figures 9c and 9d associate the electron dynamics and magnetic field to the variations of the ion beam and of the electrostatic field $\tilde{E}_x$ that is responsible for the particles' dynamics. It is clear that the main spatial fluctuation of the electron current $\tilde{j}_{ye}$ (Figure 9a) fits with the largest wavelength scale of the ion beam modulation shown in Figure 9c. Recall that the largest scale progressively dominates as time evolves. The small scales present in the ion beam are due to the early buildup of high k modes (responsible for the well-developed "tongues" in Figure 9c) and lead to much smaller amplitude fluctuations in the electron current $\tilde{j}_{ye}$ and in the electrostatic field (Figure 9d). The competitive buildup of low and high k modes versus time, and their mixing as evidenced in Figure 9c, is discussed next in section 5.

5. Inverse Cascade, Resonance Broadening, and Trapping

[27] In Figure 5, the spectrum is seen to shift from high wave number harmonics to lower wave number harmonics in what may look like an inverse cascade ending up on the first harmonic. We examine here the possible causes for this evolution. As noted in section 2 and evidenced in Figure 3, the individual growth rates among gyroharmonics are spread out: e.g., harmonic *5* has a faster rate than harmonic *1*. From this spread, one can easily understand why higher harmonics appear first and are followed by lower harmonics until the first harmonic that appears last. On the other hand, why do the higher harmonics die out first too? One may also wonder why very high harmonics such that $k\lambda_{de} > 0.6$ are not seen. An immediate approach is to investigate whether the spectral energy accumulated in the high harmonics is being transferred over the course of time to lower harmonics, as it happens in an inverse cascade. To address the question, we compared the run of Figure 5 to another run (not shown herein) that was carried out with a low-pass filter preventing the growth of waves above the first cyclotron harmonic. Of course, the electrostatic energy took longer to grow since one artificially suppressed the faster growing modes. Thus, at a given time the total electrostatic energy is smaller in the run with the low-pass filter. Smaller are also the kinetic energy lost by the ion beam and the energy gained by the electrons. However, the spectral energy contained in the first cyclotron harmonic at late time is comparable. For example, by time $\tilde{\Omega}_{ce}\tilde{t} \sim 150$ when the spectrum appears dominated by the first harmonic, the spectral energy contained in this harmonic is approximately 2×10^{-3} in both cases. Hence, we can conclude that the spectral energy does not cascade down the range of wave numbers to accumulate on the first harmonic but is reabsorbed by the particles at the level of each cyclotron harmonic (wave damping). Next, we analyze two processes which contribute to the time evolution of the electrostatic spectrum: one is resonance broadening, the other is ion trapping.

5.1. Resonance Broadening

[28] In Appendix C, we briefly recall what is resonance broadening and how it applies to electron Bernstein waves. The alternate version of the electron susceptibility valid for $k\rho_e > 1$ that we presented in section 2 (see equation (4)) is modified to become the following:

$$Q^{NL}_{xx,e} = \frac{1}{(k\lambda_{de})^2}\left\{1-\sqrt{\pi}\zeta e^{-\zeta^2}\left[\cot\left(\frac{\omega + i < \Delta\omega_k >}{\Omega_{ce}}\pi\right) - i\,\mathrm{erf}(i\zeta)\right]\right\}, \tag{11}$$

where $< \Delta\omega_k >$ denotes the resonance broadening term (equation (C2a) in Appendix C) and $\zeta \equiv (\omega + i < \Delta\omega_k >)/(\sqrt{2}k v_{te})$. In equation (11), the magnetic field appears directly via Ω_{ce} in the argument of the cot term and indirectly through $< \Delta\omega_k >$, which itself is present in ζ and in the imaginary argument of the cot term. As pointed out by *Lampe et al.* [1972], there is a very interesting limit to equation (11). For a given wave number k, once the broadening $< \Delta\omega_k >$ is large enough, the cot term tends to the constant $-i$. Hence, if the level of turbulence is sufficient so that $\Omega_{ce}/\pi \leq < \Delta\omega_k > \ll \omega$, we can replace the cot term by $-i$ while neglecting $< \Delta\omega_k >$ in ζ. As a result, the susceptibility (11) tends to that of an unmagnetized plasma. Physically, it means that the helical electron orbit is so perturbed that the phase relation between the electron and the wave k is lost after a time $\tau_D = < \Delta\omega_k >^{-1}$ lasting less than half a gyroperiod. The appropriate susceptibility, therefore, cannot anymore reflect the magnetization of the electrons. Explicitly, it becomes

$$Q_{xx,e'} = \frac{1}{(k\lambda_{de})^2}\left\{1 + i\sqrt{\pi}\zeta e^{-\zeta^2}[1 + \mathrm{erf}(i\zeta)]\right\}. \tag{12}$$

The latter can be combined with the ion susceptibility (2) into the dispersion relation $1 + Q_{xx,e'} + Q_{xx,i} = 0$, which yields the usual ion-acoustic instability (IAI). Out of brevity, we will loosely state that the electrons become "demagnetized" for that wave number k mentioned above. This demagnetization, we emphasize, concerns the high cyclotron harmonics because of the inequality $< \Delta\omega_k > \ll \omega$ and certainly does not apply to the first harmonic. In this regard, the electron susceptibility remains magnetized as evidenced by the late spectrum observed in the simulations. Note that in contrast with *Lampe et al.* [1972], who could not observe this feature since they excluded the first harmonic, the present analysis includes all gyroharmonics.

[29] It is clear from expression (C2a) that the resonance broadening is more effective on waves with large $k\rho_e$. We can therefore expect that as the simulation run develops (Figure 5), the high cyclotron harmonics with high $k\rho_e$ might be "demagnetized" first when the turbulence level is still low. Then, as the turbulence level increases, electrons interacting with gyroharmonics of progressively lower order become "demagnetized." For each gyroharmonic k present in Figure 3, we have used the electrostatic spectrum recorded in the simulation to compute $< \Delta\omega_k >$ from (C2a) and noted the time when $< \Delta\omega_k >$ reaches the value Ω_{ce}/π. Figure 10 shows the results in a diagram wave number versus time. For each gyroharmonic, a diamond labeled with italic (located at the edge of the yellow zone) marks the time of "demagnetization." Thus, harmonics *11*, *10*, *9*, etc. become "demagnetized" at early times, while harmonics *3* and *2* do so only later in the course of time. We note that a precise determination of the "demagnetization" time is difficult because of the complexity of the expression. For example, if one assumes $\zeta < 1$ as done in *Lampe et al.* [1972] in order to simplify the expression, one obtains an earlier time indicated with "X" in Figure 10. Still, the process of resonance broadening may well explain the order in which the harmonics disappear.

[30] With the chosen beam parameters (see Table 1), ion-acoustic waves are weakly unstable for $k\lambda_{de} < 0.4$ (i.e., $k\rho_e < 4$) and strongly damped for shorter wavelengths (see section 6). The marginally unstable zone is marked in Figure 10 with small pluses. We have thus three possibilities for the evolution of a given harmonic, which is illustrated by three sample cases indicated by red arrows in Figure 10. First, as shown with harmonic *7* (see the top red arrow), an acoustic wave at this short wavelength would be damped. Hence, once the electrons in the dispersion becomes demagnetized, the wave ceases to exist. Second, as shown with harmonic *3* (see the middle red arrow), an acoustic wave at this wavelength would not be damped. Hence, once the electrons become demagnetized at time $\tilde{\Omega}_{ce}\tilde{t} > 130$, the wave intensity becomes diffuse without clear spectral

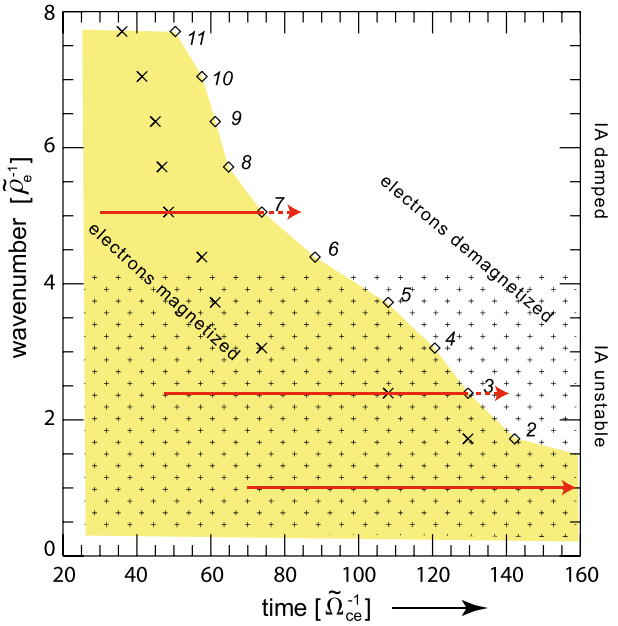

Figure 10. Time when the electrons become demagnetized in the dispersion relation according to resonance broadening. The time is indicated by a diamond shape for each harmonic (attached italic label) and is computed from the spectrum of the simulation. It progressively shifts from high to low harmonics. For reference, the crosses mark the solution of *Lampe et al*. [1972, equation (23)]. The small pluses indicate the wave number range that is weakly unstable to IA waves. The horizontal red lines at harmonics *7*, *3*, and *1* correspond to three cases discussed in the text.

feature. Last, in the case of harmonic *1* (see the bottom red arrow), the electrons remain magnetized at any time, and the wave keeps growing until another process like ion trapping saturates its growth.

[31] Resonance broadening might also provide an explanation for why harmonics with very large wave number such as harmonics *9*, *10*, and *11* are not seen in the simulation. Consider equation (C2a). The initial noise level $\sum_{k'} \frac{|E_{k'}|^2}{4\pi n T_e}$ present in the simulation might just suffice to inhibit their growth altogether. In order to test this hypothesis, we have carried out another run with 4 times more particles per grid cell, which reduced the noise level by a factor 4. Figure 11 shows the electrostatic spectrum obtained during early times. Figure 11a displays it in terms of wave number and time in a format similar to Figure 5. Axis and ordinate have only been exchanged, which allows us to show in Figure 11b an accompanying snapshot of the spectrum along the same $\tilde{k}\tilde{\rho}_e$ axis. The reduced noise level allows indeed more harmonics to appear. Harmonic *8* shows up now very clearly, while harmonics *9*, *10*, and *11* become visible, albeit faintly. We note that the global "knee" shape predicted by the linear dispersion analysis and plotted in Figure 2c is now reflected in the spectrum. Reducing the term $\sum_{k'} \frac{|E_{k'}|^2}{4\pi n T_e}$ in equation (C2a), which diminishes the broadening $< \Delta\omega_k >$ at early times, helps the emergence of modes that have both low growth rates and large wave numbers. Thus, the nonlinear effect of resonance broadening adds to the thermal effect studied in section 2.2 for damping the high gyroharmonics, thereby limiting the number of harmonics which can possibly be excited.

5.2. Ion Trapping

[32] Another way to understand the evolutionary spectral shift from high gyroharmonics to lower gyroharmonics deals with the trapping of ions forming the reflected beam. For a given level of electric field, the characteristic nonlinear time is shorter for high wave numbers than for low wave numbers as indicated by the $k\rho_e$ dependence in equation (10). Thus, the high harmonics that grow early are also the first to initiate some ion trapping, as evidenced in Figure 6a. Now, the same beam ions are also resonant with lower harmonics. As time evolves and the lower harmonics reach sufficient intensity to also begin ion trapping, the coherence previously established between the ions and the high harmonics becomes lost. In Figure 6b, one can see that several different wavelengths are at play simultaneously. As small-scale structures of the ion phase space (higher harmonics) are displaced by larger-scale structures (lower harmonics), the spectral energy contained in high $k\rho_e$ values drops (strong damping). Figure 6c clearly shows structures of shorter scales being carried away by the trapping associated with the first harmonic. Thus, what looks like an inverse cascade is the result of the formation of a "broth" of vortices of different spatial scale which have a different evolutionary time scale.

6. Ion-Acoustic versus Electron Cyclotron Drift Instability

[33] Other instabilities have been studied in the context of the shock's foot and the relative drift of its different local populations. In Figure 12, we compare the growth rate of ion-acoustic instability (IAI) to that of the ECDI for our set of plasma parameters (see Table 1). The IAI, which is shown here with a green line, is marginally unstable for wave numbers $k\lambda_{de} < 0.45$ and strongly damped for shorter wavelengths. Since the modified two-stream instability (MTSI) has lately returned to the fore thanks to recent studies [*Scholer et al.*, 2003; *Matsukiyo and Scholer*, 2003, 2006; *Umeda et al.*, 2012], we also show it here for further comparison. In the little insert on the left, its growth rate is indicated schematically for the optimal conditions of *Matsukiyo and Scholer* [2003, Figure 4], namely $\theta = 85°$, $M/m = 1836$, and $\beta_e = \beta_i = 0$. It clearly has a much longer wavelength and a much smaller growth rate than the ECDI. In spite of its weak growth rate relative to the ECDI, the instability is important because it involves the dynamics of the electrons along the magnetic field lines and allows for their parallel heating. We note that the total time span of our simulations corresponds to $180/\Omega_{ce}$, namely $3/\gamma_{MTSI}$. This instability would thus hardly have the time to grow if our simulation design had allowed for it.

[34] In order to compare and contrast features of the IAI with those of the ECDI, we carried out another run with the parameters of Table 1 except for the ambient B_o field that was set to zero. Figure 13 compares the spectra obtained in either case. The ECDI spectrum at $\tilde{\Omega}_{ce}\tilde{t} = 60$ (beginning of stage T2) is displayed in Figure 13a. Peaks at harmonics *3*, *4*, *5*, *6*, and *7* are well visible and much above the level

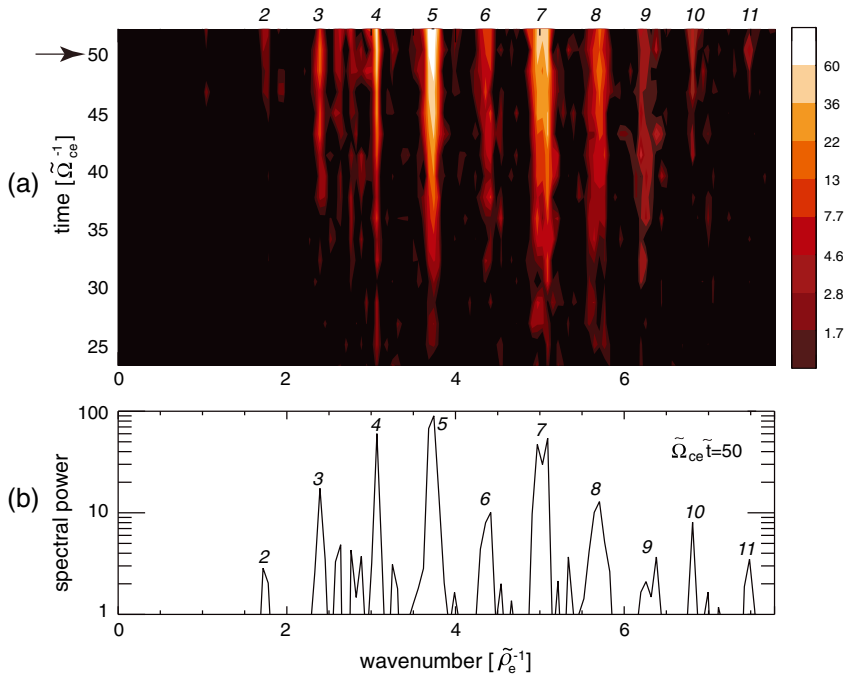

Figure 11. (a) Early evolution of the electrostatic energy spectrum for an extra simulation run with 1600 particles/cell for each population. All other parameters are as in the reference run (cf. Table 2); hence, Figure 11a can be compared with stage T_1 of Figure 5. Italicized figures label the Bernstein harmonics. Note the global "knee" shape reflecting the growth rates shown in Figure 2c. (b) Snapshot at time $\tilde{t} = 50\tilde{\Omega}_{ce}^{-1}$ indicated by an arrow on the LHS of Figure 11a.

of the broad IAI spectrum which is shown in Figure 13c at the same time for comparison. A late ECDI spectrum (Figure 13b) is to be compared with the IAI spectrum at the same time (Figure 13d). We use a logarithmic scale in order to focus on features besides the intense peak at $\tilde{k}\tilde{\lambda}_{de} = 0.09$ associated with the first gyroharmonic. Clearly, the ECDI spectrum is broadly enhanced around $\tilde{k}\tilde{\lambda}_{de} \sim 0.1$. However, beyond $\tilde{k}\tilde{\lambda}_{de} > 0.2$, there is no significant difference between the spectra produced by the two simulation runs.

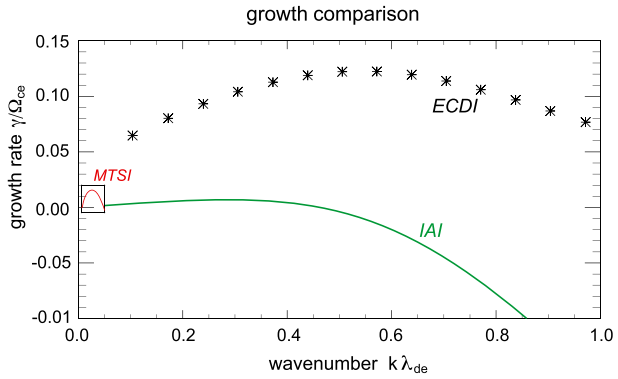

Figure 12. Growth rate of the ion-acoustic instability (IAI) from solving the linear dispersion with unmagnetized electron susceptibility (see equation (12)). Maximal growth rates of the ECDI for each gyroharmonic (obtained from Figure 2c) are marked with asterisks for reference. An insert shows the MTSI in red for comparison.

[35] By contrast, the late particle phase space evidences a very different picture between the ECDI run and the IAI run, as demonstrated in Figure 14. Here, we focus on a short portion of the simulation box spanning $20\tilde{\rho}_e$ and compare the $[\tilde{x}, \tilde{v}_x]$ spaces of the electrons (Figures 14a and 14b) and of the beam's ions (Figures 14c and d). Electrons are significantly heated in the ECDI case (Figure 14a), as already noted about Figure 4 and explained in Appendix B by their strong response to the electric field of the first gyroharmonic. In the IAI case, they heat much less (Figure 14b) because the spectrum is weak and broad without any particular resonance. Interestingly, we note the presence of electron holes (e.g., there are clear ones at $\tilde{x} = 16\tilde{\rho}_e$, $25\tilde{\rho}_e$, and $28.5\tilde{\rho}_e$). Electron holes can form because no gyrating component affects the one-dimensional electron motion driven by the E_x-field. Regarding the ion beam, we can see that it is very strongly affected in the ECDI case (Figure 14c), unlike in the IAI case (Figure 14d) where it is only lightly affected by the weak and broad spectrum that is displayed in Figure 13d.

7. Discussion

[36] The present study is focused on wave activity developing within the foot region of a supercritical perpendicular shock, where three different particle populations interact and are the sources of microinstabilities. Although the approach used herein does not simultaneously include the full dynamics of the shock itself, it offers the advantage of a very detailed analysis of the wave activity with high spatial/time resolution and high particle statistics. For the global picture, the successive nonlinear stages which are evidenced herein

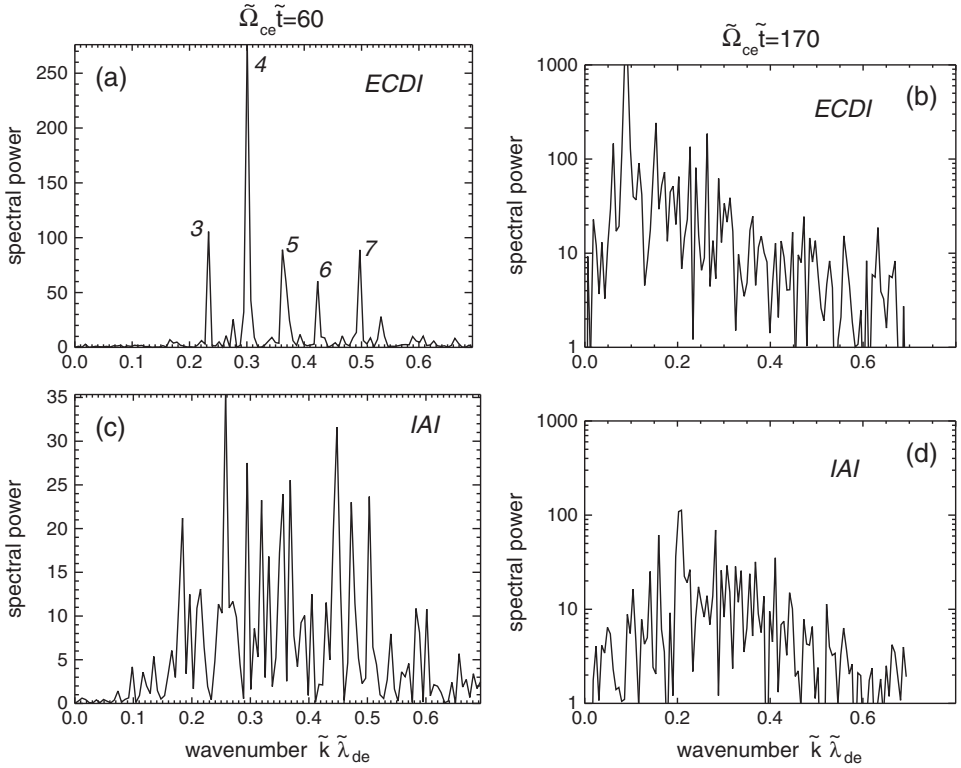

Figure 13. Snapshots of the electrostatic energy spectrum at two times, $\tilde{\Omega}_{ce}\tilde{t}$ = 60 and 170, comparing two different simulation runs: (a, b) ECDI reference run with $\tilde{B}_0$ = 5 and (c, d) IAI run with $\tilde{B}_0$ = 0. Apart from $\tilde{B}_0$, other parameters are identical (cf. Table 2).

for the first time need to be re-inserted within the larger frame of evolving shock front structures.

[37] First, we must take into account that these structures vary in time when the shock front self-reforms. Yet, all the processes described in this paper occur very quickly over a time on the order of the lower hybrid period. By contrast, the self-reformation time is on the order of the ion cyclotron period, namely a factor $\tau_{ci}/\tau_{lh} = \sqrt{M/m}$ longer. It is also noteworthy that the growth rate given in (8) is such that $\gamma/\Omega_{ci} \sim (M/m)^{3/4}$. As the mass ratio increases to realistic values, the instability has more time to develop. One may therefore expect that the processes described herein are minimally affected by the evolution of the shock front (nonstationarity) and that their nonlinear characteristics should have plenty of time to emerge before the original narrow beam of reflected ions has disappeared.

[38] Second, we must consider the effects of convection. Remember that the simulations are performed in a frame where the electrons are at rest. Seen from the shock frame, the electrons drift toward the shock front with a speed V_e that is related to the solar wind speed V_1 by equation (6) of *Muschietti and Lembege* [2006], namely

$$V_e = V_1(1 - 2\alpha + 2\alpha/r), \tag{13}$$

where α is the relative ion density in the beam and r is the shock's compression ratio. One needs to compare the distance covered by the drifting electrons during a lower hybrid period $\tau_{lh}V_e$ with a characteristic length of the foot region. The latter is commonly evaluated as $L_f = V_1/\Omega_{ci}$. Using equation (13), one obtains

$$\tau_{lh}V_e = L_f \left[2\pi(1 - 2\alpha + 2\alpha/r)\sqrt{m/M}\right]. \tag{14}$$

Considering that the factor in bracket is approximately 0.2 for the chosen parameters and would further decrease for a realistic mass ratio, our scenario appears quite reasonable even when being inserted within the full dynamics of a supercritical perpendicular shock. On the other hand, convection effects are likely important and should be accounted for in a more complete study. Lastly, even though the paper's title refers to perpendicular shock, we note that the ECDI would also develop where shocks are not strictly perpendicular. The preferred wave vector would then point to a direction perpendicular to $\mathbf{B_0}$ within the coplanarity plane.

[39] We now turn to compare the present main results with previous works. Our former study [*Muschietti and Lembege*, 2006], which included the full dynamics of the shock and its self-reformation, had first evidenced the development of the electron cyclotron drift instability (ECDI) within the foot region. However, the parameter regime was far from realistic, partly due to numerical conditions and partly in order to mimic the parameters in *Hada et al.* [2003]. By contrast, the present work uses a more realistic parameter regime. Ion and electron scales are now widely separated thanks to a mass ratio M/m = 400 (instead of 100), and the Debye length is considerably smaller than the electron gyroradius thanks to ω_{pe}/Ω_{ce} = 10 (instead of 2). As a result, the upper hybrid branch is well separated from the

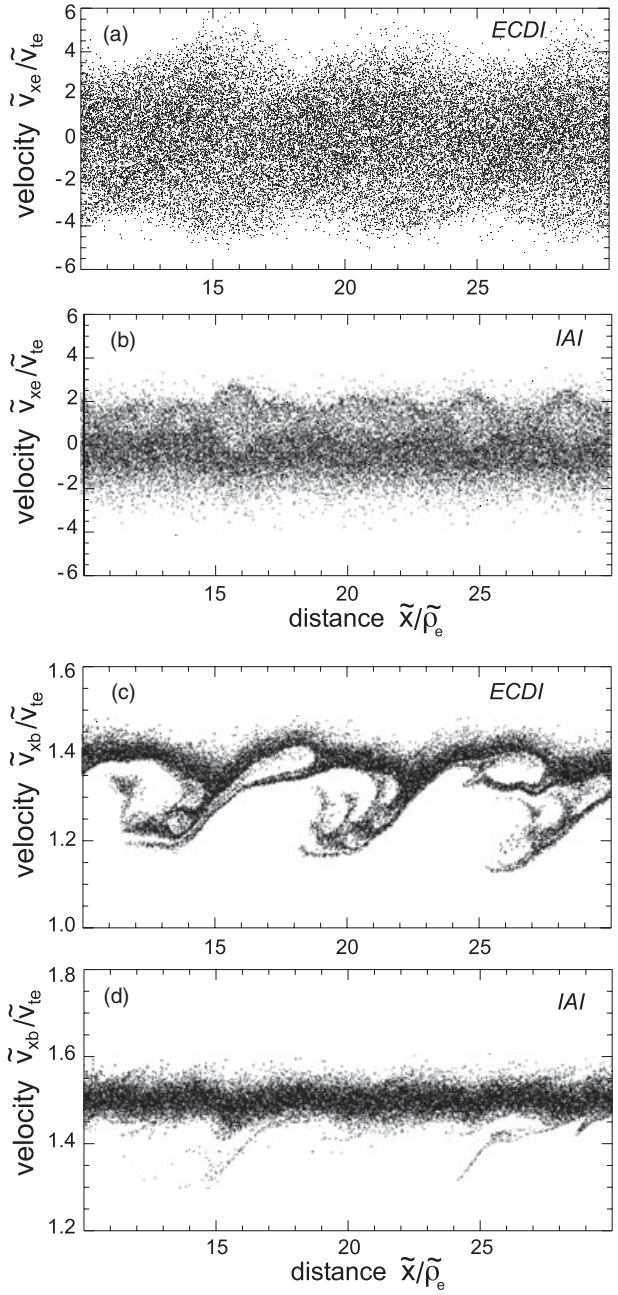

Figure 14. Snapshots of the phase space $[\tilde{x}, \tilde{v}_x]$ at $\tilde{\Omega}_{ce}\tilde{t}$ = 170 which compare the behavior of (a, b) the electrons and (c, d) the beam ions for the two different simulation runs of Figure 13: ECDI and IAI. Note the substantial heating of the electrons in the ECDI case (in Figure 14a) and the modest alteration of the ion beam in the IAI case (in Figure 14d).

first Bernstein branch. The present work confirms the strong persistence of the ECDI when approaching more realistic parameters. Moreover, it shows that the ECDI can excite many harmonics belonging to purely backward propagating branches below the upper hybrid branch. In *Muschietti and Lembege* [2006], the first gyroharmonic only was observed, which can be ascribed to physical and numerical reasons. Numerically, the present periodic conditions allow to use a better grid with resolution down to the Debye length and better particle statistics with less numerical noise. Physically, the number of harmonics excited is indeed expected to increase for a larger ratio ω_{pe}/Ω_{ce}, as explained near the end of section 2.1. In addition, the large value of ω_{pe}/Ω_{ce} used herein and hence the separation of the upper hybrid branch from the first Bernstein branch allows to clarify the following. The present ECDI should not be confused with the so-called Buneman instability (BI) which has been promoted by *Shimada and Hoshino* [2000] and which operates for drift velocities of the ion beam V_b very large as compared with the electron thermal speed v_{te}, in contrast to the ECDI. The fact that the electron cyclotron frequencies discussed in the present paper are well below the upper hybrid frequency establishes unambiguously that the ECDI is not a magnetized variant of the Buneman instability. As a matter of fact, the reflected ion beam used herein (see Table 1) is absolutely not Buneman unstable. It can barely excite an ion-acoustic instability as shown in Figure 12. We emphasize this point because the BI has been reported [*Shimada and Hoshino*, 2000] to occur in simulations of supercritical shocks with an Alfven Mach number $V_1/V_A \gtrsim 10$. However, the BI regime, namely the beam speed $V_b \approx 2V_1 = 2M_A V_A >> v_{te}$, occurs easily in simulations using a small mass ratio. Indeed, because

$$v_{te} = (\beta_e/2)^{1/2}(M/m)^{1/2}V_A, \tag{15}$$

the electron thermal speed v_{te}, which is just a few times V_A for strongly reduced mass ratio, becomes much larger for realistic mass ratios. In *Shimada and Hoshino* [2000], e.g., the simulations had $\beta_e = 0.15$ and $M/m = 20$, which yields $v_{te}/V_A = 1.7$. In this paper, the ratio is $v_{te}/V_A = 4$, and in an ideal simulation with realistic mass ratio, it would be of order 10. Thus, as the mass ratio increases toward a realistic value, the range of Mach numbers where the present ECDI applies expands, while the range where the BI applies shifts toward very high Mach values that do not concern Earth's bow shock. In a later paper, *Shimada and Hoshino* [2004] performed new simulations with a realistic mass ratio, $M/m = 1836$, an improvement which was partially offset by a small electron temperature, $\beta_e = 0.01$, resulting in a ratio $v_{te}/V_A = 3$. In spite of this rather modest ratio, the Mach number was set to $M_A = 16$ so as to fully satisfy the criterion for the Buneman instability. Yet again, although relevant for astrophysical shocks, such a regime is not suitable for planetary shocks considered in the present study.

[40] If one considers wave propagation directions that are off the perpendicular to the ambient magnetic field $\mathbf{B_o}$, the modified two-stream instability (MTSI) [*McBride et al.*, 1972], or its generalized electromagnetic variant the"kinetic cross-field streaming instability" [*Wu et al.* 1984, sec. 3.1.3], is important and easy to excite since it operates for a drift velocity less than the electron thermal speed $\sqrt{T_e/m}$. The unstable frequency lies between the ion and electron gyrofrequencies, so that one assumes the ions as unmagnetized but electrons as magnetized. The electrons can, however, freely move in the wave propagation direction thanks to a wave vector's component along $\mathbf{B_o}$ that is small yet finite. *Scholer et al.* [2003] performed 1-D PIC simulation of a shock with $\theta_{Bn} = 87°$ and identified a MTSI resulting from the relative drift between incoming ions and

electrons in the foot region. Later, *Matsukiyo and Scholer* [2006] performed a periodic 2-D PIC simulation of microinstabilities in the foot region and identified a second MTSI which results from the relative drift between reflected ions and electrons. The 2-D simulation design equally allowed for wave propagation perpendicular to $\mathbf{B_o}$ and so the development of the ECDI. Early on in their simulation, these authors did indeed observe the ECDI yet confused it with the Buneman instability. For $\omega_{pe}/\Omega_{ce} = 2$ (value chosen by the authors), the upper hybrid branch, where the BI is expected to occur, is the second harmonic and thus close to the first harmonic. This made it difficult to distinguish the ECDI from a Buneman type of instability. Due to the ratio $\omega_{pe}/\Omega_{ce} = 2$, they could of course not observe the successive nonlinear stages which are described in the present paper and characterize the apparent "inverse cascade." Generally, as compared to the MTSI, whose growth rate is on the order of the lower hybrid frequency, the ECDI growth is faster. On the other hand, for a beam drift $V_b < \sqrt{T_e/m}$, a regime favorable for the MTSI, the wave intensity reached by the ECDI is modest. The waves might be difficult to identify in a noisy PIC simulation. Moreover, the wavelengths involved can be quite short depending upon the chosen parameters. As explained in *Muschietti and Lembege* [2006, see equation (12)], the wave number $k\lambda_{de} \sim (v_{te}/V_b)(\Omega_{ce}/\omega_{pe})$. If the simulation's parameters are such $v_{te} > V_b$ while the frequency ratio ω_{pe}/Ω_{ce} is not large, the wavelength may be just too short for the simulation's grid.

[41] Although it is interesting to see the MTSI-1 and MTSI-2 occurring in succession [*Matsukiyo and Scholer*, 2006], associated first with the incoming ions and second with the reflected ions, one may wonder what convection's effects would do to this scenario. Indeed, the simulation is performed with a periodic code, takes place in the rest frame of the electrons, and therefore is subjected to the same caveat as ours regarding the neglected effects of convection. If, as we did with equation (14), one attempts to reinsert these authors' results within the framework of a supercritical shock and computes the distance covered by the drifting electrons during the total period τ_{sim} of their simulation, one obtains $\tau_{sim} V_e = 0.4 L_f$, which barely justifies neglecting convection in a first approach. In fact, a recent work has examined the two MTSI's role within the framework of an evolving shock [*Umeda et al.*, 2012], which automatically includes convection effects. Although these 2-D simulations of a perpendicular shock evidenced the MTSI-2, the MTSI-1 was not clearly observed, which the authors attributed to convection effects limiting its growth.

[42] Several results presented herein confirm the early work of [*Lampe et al.*, 1972]. The major difference is that we use a fully electromagnetic code (instead of electrostatic) and that our modern simulation design enables us to excite several gyroharmonics while simultaneously resolving well the relatively long-wavelength first harmonic. Consequently, we can recognize the apparent "inverse cascade," as exhibited in Figure 5, and can analyze the underlying processes. In the late stage, the spectrum is completely dominated by the first harmonic at $k\rho_e \approx 1$ in sharp contrast to the broad acoustic spectrum around $k\lambda_{de} \sim 1$ described by *Lampe et al.* [1972]. Furthermore, we find that this late spectrum has a substantial magnetic component which was of course absent in these authors' results since their code was electrostatic. Lesser yet significant differences are in the parameter choice. These authors use a denser ($\alpha = 0.5$) and colder ($T_b = T_e/100$) reflected ion "beam" which does not apply well to planetary shocks.

[43] So far, there have been scant observations of electron cyclotron harmonics in association with shocks. Only one paper to our knowledge [*Wilson et al.*, 2010] reports Bernstein-like waves observed at a supercritical interplanetary shock. In the magnetosphere, though, electron cyclotron harmonic waves have been often measured, e.g., by Geotail [*Usui et al.*, 1999], and could be destabilized by an ion beam [*Brinca et al.*, 2003] similar to the scenario described herein.

8. Conclusions

[44] We have analyzed the source mechanisms responsible for wave activity within the foot region of a supercritical perpendicular shock. The present study, which is one dimensional, is focused on the wave activity developing along the shock normal and triggered by the interaction of the three particle components that coexist within the foot region: incoming electrons/ions and reflected ions. For perpendicular propagation, the electron cyclotron drift instability (ECDI), which results from the relative drift between the reflected ions and the electrons, has been identified as the source mechanism of electron Bernstein waves. We summarize the main results concerning this instability hereafter.

[45] In the linear stage of 1-D PIC simulations, discrete bands of emission, a characteristic signature of the ECDI, are recovered in agreement with solutions obtained separately from wave dispersion analysis. In this stage, the waves are mainly electrostatic, and the growth of the different gyroharmonics resulting from the interaction with the reflected ion beam takes place on different time scales in good agreement with dispersion analysis. The number of gyroharmonics excited, while proportional to the drift, is limited by kinetic effects (finite ion beam temperature) that affect more the very high k modes and degrade their growth. In addition, the process of resonance broadening is shown to play a role. It applies even at early times and further suppresses very high harmonics. In this sense, there is no "linear" stage, strictly speaking, in the analysis of our numerical simulation results.

[46] As for the subsequent nonlinear evolution, the most salient features revealed in the present study are as follows:

[47] 1. The discrete band-type emission progressively shifts from high harmonics to lower harmonics in what may look like an "inverse cascade." Eventually, most of the wave electrostatic energy is stored at the lowest electron gyroharmonic. This evolutionary shift takes place within a time scale around the lower hybrid period.

[48] 2. We have analyzed in detail the causes behind the spectral evolution and found two complementary processes at play: resonance broadening and ion trapping. The relative efficiency of each process varies depending upon the time of the simulation run and upon which of the different k modes is concerned. A diagram shown in Figure 15 summarizes the role of each process in the course of the simulation. The end result always is a "broth" of different k modes of low spectral intensity dominated by an intense first harmonic at wave number $k\rho_e \approx 1$ and frequency $\omega \approx \Omega_{ce}$.

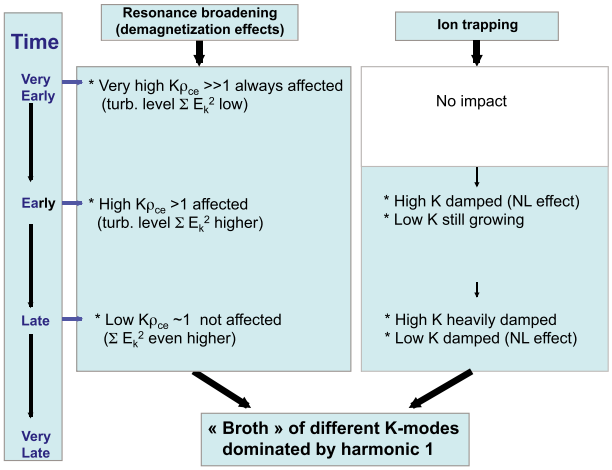

Figure 15. Diagram which summarizes the relative efficiency of resonance broadening versus ion trapping in shaping the spectral evolution observed in the simulation (Figure 5).

[49] 3. A striking feature is the buildup of a magnetic component during the late stage. Since the ECDI is generally considered as an electrostatic instability, this widely held view should be revised at least concerning its nonlinear evolution. The magnetic field component B_z takes place at the lowest harmonic branch (Ω_{ce}). Its growth is supported by a significant electron current J_{ye} which occurs when a large Bernstein wave develops on this low harmonic branch. Indeed, electrons respond strongly to an electric field at their cyclotron frequency. We have shown that electrons from the core of the distribution can be momentarily trapped in the electrostatic potential of the Bernstein wave and pick up energy from the motional electric field which accelerates them in the $\hat{y}$ direction. The process, which is reminiscent of the shock drift type acceleration (SDA) familiar for ions, gives birth to a substantial current J_{ye}.

[50] 4. Through their participation in the ECDI, the electrons experience some heating. In particular, their acceleration during the late stage leads to the formation of a local distribution function that has a flat top in $v_\perp$. This is evidence that some preheating of electrons can occur within the foot region even for a strictly perpendicular shock.

[51] 5. The ECDI has been compared to the IAI. Although the wave energy level is similar, the ECDI concentrates the spectral energy in discrete bands, first at multiple gyroharmonics and eventually at the first gyroharmonic. This discretized spectrum turns out to be much more efficient than the broad acoustic spectrum of the IAI for tapping energy from the ion beam and energizing the electrons.

[52] 6. The ECDI has been briefly compared with features of the MTSI. Our results show that the ECDI can easily be excited over a time range much shorter than the lower hybrid period τ_{lh}, in contrast to the MTSI which grows around τ_{lh}.

[53] 7. The electron kinetic energy gain is comparable to the loss of the ion beam energy. At any time, the energy in the ECDI remains a very small fraction of the energy transferred from the ion beam to the electrons. In other words, the ECDI is mainly a "conduit" to transfer energy from the ion beam to electrons.

[54] All the features above take place very shortly, namely over a time scale slightly above the lower hybrid period, which is much less than any time scale characteristic of the shock dynamics itself: (a) the upstream ion gyroperiod which characterizes the ion reflection and (b) the self-reformation cyclic period which characterizes the nonstationarity of the whole shock front (ramp and foot). Taking into account the convection effect due to the solar wind motion, this wave activity (in terms of both electric and magnetic fields) that originates from the foot region may pollute the ramp region and contribute to the wave activity within the overall shock front.

[55] Finally, a comparative study with previous works has been performed and confirms that these features have not been observed hitherto, mostly due to a lack of spatial and time resolution. At present, the study is based on perpendicular propagation only. A parametric study is under active investigation in order to establish the link with other microinstabilities that are also responsible for wave activity within the shock front but in conditions different from those considered herein.

Appendix A: Magnetic Signature of the Waves

[56] Conductivity tensor σ and susceptibility Q of linear wave theory are closely related. The cross-field conductivity σ_{yx}, which stems from the magnetized motion of the electrons, expresses the linear response in the $\hat{y}$ direction due to a nominal electric field in the $\hat{x}$ direction, $j_y = \sigma_{yx}E_x$. In the case of electron Bernstein waves, it reads

$$\sigma_{yx} = \frac{\Omega_{ce}}{4\pi}\frac{\omega_{pe}^2}{\Omega_{ce}^2}\left[\Lambda_1(\eta) - \Lambda_0(\eta) + \sum_{n=1}^{\infty}\frac{\omega^2}{\omega^2 - n^2\Omega_{ce}^2}\left(\Lambda_{n+1}(\eta) + \Lambda_{n-1}(\eta) - 2\Lambda_n(\eta)\right)\right], \tag{A1}$$

where the modified Bessel functions Λ_n and their arguments $\eta \equiv (k\rho_e)^2$ are the same as in equation (1). Figure A1 displays the values of $-\sigma_{yx}$ for successive Bernstein harmonics.

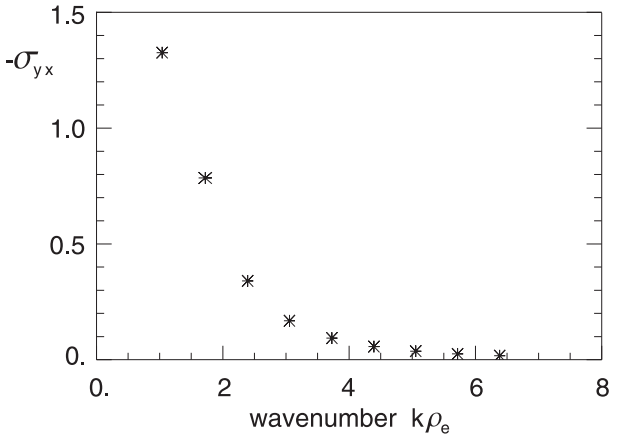

Figure A1. Cross-field conductivity σ_{yx} versus dimensionless wave number $k\rho_e$. Equation (A1) is used to plot the conductivity for successive Bernstein harmonics (see text of Appendix A).

For each harmonic, we numerically solve the dispersion relation to determine the pair (k, ω) at maximum growth. This pair is then used to evaluate (A1) and place an asterisk on the plot. It is clear that the cross-field conductivity diminishes quickly with increasing wave number.

Appendix B: Orbits of Electrons in a Bernstein Wave

[57] In this appendix, we consider a Bernstein wave propagating in a direction $\hat{\mathbf{x}}$ perpendicularly to the ambient magnetic field $\hat{\mathbf{z}}B_o$ and investigate the resulting motion of an electron in the plane $[x, y]$. To eliminate all explicit time dependence, we work in the wave frame moving with the phase speed $u_w \mathrm{v_{te}}$ in the $\hat{\mathbf{x}}$ direction. In dimensionless form where Ω_{ce}^{-1} and ρ_e are the units of time and distance, respectively, the dynamical equations for the electron can then be written as

$$\begin{aligned} \dot{v}_x &= -v_y[1 - \delta b_z \sin(kx + \varphi)] - \delta a_x \cos(kx + \varphi) \\ \dot{v}_y &= +v_x[1 - \delta b_z \sin(kx + \varphi)] + u_w. \end{aligned} \tag{B1}$$

The term $\delta a_x \equiv (c/\mathrm{v_{te}})(E_x/B_o)$ is the dimensionless acceleration due to the wave electric field. As we have seen in section 4 (Figures 4d and 8), the simulation evidences a fluctuating, self-consistent magnetic component $\mathrm{B_z}$ in addition to the ambient field B_o. This component is $\pi/2$ out of phase with the electric field and accounted for here by a term $\delta b_z \equiv (1/B_o)B_z$. Integrating the dynamical equations (B1) numerically with values for E_x and B_z taken from the simulation during stage $\mathrm{T_3}$ ($\delta a_x = 2$, $\delta b_z = 0.02$, $u_w = 1.3$, and $k = 1$) shows that some electrons from the core of the distribution can be significantly energized. A temporary trapping in the electrostatic potential of the wave and the associated motion in the $\hat{\mathbf{y}}$ direction enables the motional electric field $E_y = -B_o(u_w \mathrm{v_{te}}/c)$ to effect some work on the particles [*Goodrich and Scudder*, 1984]. Figures B1a, B1b, and B1c display the orbit of such an electron together with the profile of the potential $-\phi(x) = \int^x E_x(x')\mathrm{d}x'$ shown for reference. The three panels show the orbit in $[x, y]$, $[x, v_x]$, and $[x, v_y]$ space, respectively. The small case letters "a," "b," "c," "d," "e," and "f" identify the electron's successive locations on the orbit. The particle is seen to move in x from right to left because the view is from the wave frame. It starts at "a" with velocities $(v_x, v_y) = (-1.3, 1.)$ and moves to "b" where it is reflected by the potential, i.e.,, where $(v_x, v_y) = (0, 0)$. The electron then begins an important excursion in y and is accelerated by the motional electric field until point "c" where the y velocity reaches a maximum, $v_y \approx 4$. Due to the Lorentz force, this large velocity is progressively transferred from v_y to v_x, while the drift in y continues at a reduced clip until point "d" where the kinetic energy of the electron is maximum. One can easily evaluate the energy gain by computing the work done by the motional electric field over the particle's excursion in y. One obtains $u_w \times \Delta y = 1.3 \times 11 = 14.3$.

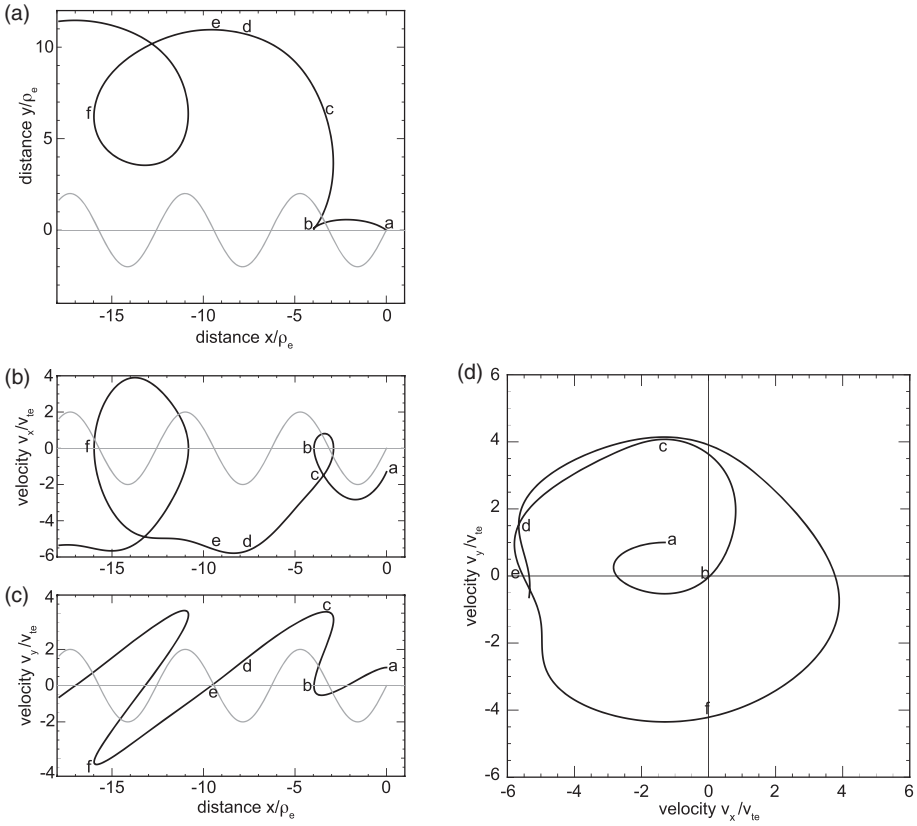

Figure B1. Phase-space orbit of an electron as seen from the rest frame of a large Bernstein wave. In grey, the electrostatic potential of the wave. (a) Solution in $[x, y]$ of equation (B1) with wave field values $\mathrm{E_x}$ and $\mathrm{B_z}$ typical of stage $\mathrm{T_3}$ of the simulation. Corresponding variations of the two velocity components (b) $[x, v_x]$ and (c) $[x, v_y]$. (d) Phase-space orbit in $[v_x, v_y]$ of the electron showing its acceleration to a large gyro-orbit. For description, see text of Appendix B.

Hence, a thermal electron can reach a large energy over 14 times its initial energy. At point "e," v_y changes sign and becomes negative. Its amplitude then increases until point "f" where $v_y \approx -4$. We note that the change from $v_y \approx +4$ to $v_y \approx -4$ takes place over a distance well over one wavelength. The electron has been accelerated and its gyroradius substantially increased, as visible in Figure B1d. The orbit in $[v_x, v_y]$ space demonstrates how the particle which originally belongs to the core of the distribution is at point "b" kicked out from the core to reach a larger gyro-orbit with $v_\perp \approx 4$. A similar energization process for the electrons can occur where they are blocked by ion phase-space holes that move perpendicularly to $\hat{\mathbf{z}}B_o$. *Shimada and Hoshino* [2004] invoked the motional electric field present in the rest frame of the ion holes to account for a strong energization of the electrons observed in their simulation.

Appendix C: Resonance Broadening and Nonlinear Electron Susceptibility

[58] In conventional plasma theory, one uses linear orbits to integrate Vlasov equation and obtain the dispersion relation. For example in a magnetized plasma, the electrons' linear orbits consist of gyrocenters that follow the magnetic lines at constant speed, of constant gyroradii, and of gyrophases varying as $\Omega_{ce}t$. In Dupree's theory of strong turbulence [*Dupree*, 1966], the orbits take place in a turbulent medium and are subjected to random forces. The effect of the latter on the electrons is described in terms of diffusion and causes the phase relation between an electron and a wave to be destroyed after a time τ_D. This finite interaction time corresponds to a broadening of the usual wave-particle resonance in the frequency domain, $\Delta\omega_k = \tau_D^{-1}$. For gyro-orbits in a magnetized plasma, the diffusion has three origins: a cross-field Brownian motion of the gyrocenters, random changes in the gyroradii, and random changes in the phase angles [*Dum and Dupree*, 1970]:

$$\Delta\omega_k = k_\perp^2 \left[\frac{1}{k_\perp^2} \mathbf{k} \cdot \mathbf{D}_\perp \cdot \mathbf{k} + \frac{1}{2\Omega_{ce}^2}(D_{v_\perp v_\perp} + D_{\phi\phi}) \right]. \quad \text{(C1)}$$

An expression for $\Delta\omega_k$ in terms of the spectral intensity has been obtained by *Dum and Dupree* [1970] in the case of an isotropic spectrum. The expression has been adapted by *Lampe et al.* [1972] for a one-dimensional spectrum perpendicular to $\mathbf{B_o}$ such as generated by the electron cyclotron drift instability. It depends upon the wave number and the gyroradii (i.e., the perpendicular velocities) of the electrons and hence needs to be averaged over a velocity distribution before it can be used in a dispersion relation: $<\Delta\omega_k>= \int d^3v f_e \Delta\omega_k(v_\perp)$. The averaged expression obtained by *Lampe et al.* [1972, see (18)] is

$$\frac{<\Delta\omega_k>}{\Omega_{ce}} = \left(\frac{1}{2}\right)^{7/2} \left(\frac{\omega_{pe}}{\Omega_{ce}}\right)^2 k\rho_e \sum_{k'} \frac{|E_{k'}|^2}{4\pi n T_e} \frac{k}{k'} \mathrm{Im}[G(\zeta_+) + G(\zeta_-)], \quad \text{(C2a)}$$

where we write $G(\zeta_\pm)$ in terms of erf function (rather than the Z function used by the authors)

$$G(\zeta_\pm) \equiv 2\sqrt{\pi} e^{-\zeta_\pm^2} \left[-\cot\left(\pi \frac{\omega + i <\Delta\omega_{k'}>}{\Omega_{ce}}\right) + i\,\mathrm{erf}(i\zeta_\pm) \right] \quad \text{(C2b)}$$

and

$$\zeta_\pm \equiv \frac{\omega \pm \Omega_{ce} + i <\Delta\omega_{k'}>}{\sqrt{2}k' v_{te}}. \quad \text{(C2c)}$$

Once the effects of the turbulent electric fields on the gyro-orbits are lumped in $<\Delta\omega_k>$, the nonlinear electron susceptibility for Bernstein waves simply becomes

$$Q_{xx,e}^{NL} = -\frac{1}{k^2\lambda_{de}^2} \left[-1 + \Lambda_0(\eta) - 2\sum_{n=1}^{\infty} \Lambda_n(\eta) \frac{(\omega + i <\Delta\omega_k>)^2}{n^2\Omega_{ce}^2 - (\omega + i <\Delta\omega_k>)^2} \right], \quad \text{(C3)}$$

which is to be compared to equation (1). Now, regarding the size of the broadening $<\Delta\omega_k>$, from (C2a) we note that, first, it is proportional to the spectral level and, second, it affects more large values of $k\rho_e$, hence the higher gyroharmonics which are excited by the ECDI.

[59] **Acknowledgments.** The one-dimensional PIC simulations have been performed on the supercomputer of IDRIS center located at Orsay (near Paris). The work has been partially performed while one of the authors (LM) was staying at LATMOS (France), which is thanked for its hospitality and the access to computing facilities. The research work was supported by NASA under grant NNX10AL09G to UC Berkeley.

References

Biskamp, D., and H. Welter (1972), Numerical studies of magnetosonic collisionless shock waves, *Nucl. Fusion*, *12*, 663.

Brinca, A. L., F. J. Romeiras, and L. Gomberoff (2003), Stimulation of electron Bernstein modes by perpendicular ion beams, *Geophys. Res. Lett.*, *30*, 2175–2178, doi:10.1029/2003GL017501.

Chapman, S. C., R. E. Lee, and R. O. Dendy (2005), Perpendicular shock reformation and ion acceleration, *Adv. Space Res.*, *121*, 5–19, doi: 10.1007/s11214-006-4481-x.

Dum, C. T., and T. H. Dupree (1970), Nonlinear stabilization of high-frequencies instabilities in a magnetic field, *Phys. Fluids*, *13*, 2064–2081.

Dum, C. T. (1989), Transition in the dispersive properties of beam-plasma and two-stream instabilities, *J. Geophys. Res.*, *94*, 2429–2442.

Dupree, T. H. (1966), A perturbation theory for strong plasma turbulence, *Phys. Fluids*, *9*, 1773–1782.

Fried, B. D., and S. E. Conte (1961), *The Plasma Dispersion Function*, Academic Press, New York.

Goodrich, C. C., and J. D. Scudder (1984), The adiabatic energy change of plasma electrons and the frame dependence of the cross-shock potential at collisionless magnetosonic shock waves, *J. Geophys. Res.*, *89*, 6654.

Hada, T., M. Oonishi, B. Lembege, and P. Savoini (2003), Shock front nonstationarity of supercritical perpendicular shocks, *J. Geophys. Res.*, *108*, 1233, doi:10.1029/2002JA009339.

Lampe, M., W. M. Mannheimer, J. B. McBride, J. H. Orens, K. Papadopoulos, R. Shanny, and R. N. Sudan (1972), Theory and simulation of the beam cyclotron instability, *Phys. Fluids*, *15*, 662–675.

Lembege, B., and J. M. Dawson (1987), Self-consistent study of a perpendicular collisionless and nonresistive shock, *Phys. Fluids*, *30*, 1767–1788.

Lembege, B., and P. Savoini (1992), Nonstationarity of a two-dimensional quasiperpendicular supercritical collisionless shock by self-reformation, *Phys. Fluids*, *B4*, 3533–3548.

Matsukiyo, S., and M. Scholer (2003), Modified two-stream instability in the foot of high Mach number quasi-perpendicular shocks, *J. Geophys. Res.*, *108*, 1459–1469, doi:10.1029/2003JA010080.

Matsukiyo, S., and M. Scholer (2006), On microinstabilities in the foot of high Mach number perpendicular shocks, *J. Geophys. Res.*, *111*, A06104.

McBride, J. B., E. Ott, J. P. Boris, and J. H. Orens (1972), Theory and simulations of turbulent heating by the modified two-stream instability, *Phys. Fluids*, *15*, 2367–2383.

Muschietti, L., and B. Lembege (2006), Electron cyclotron microinstability in the foot of a perpendicular shock: A self-consistent PIC simulation, *Adv. Space Res.*, *37*, 483–493, doi:10.1016/j.asr.2005.03.077.

Nicholson, D. R. (1983), *Introduction to Plasma Theory*, John Wiley, New York.

Scholer, M., I. Shinohara, and S. Matsukiyo (2003), Quasi-perpendicular shocks: Length scale of the cross-shock potential, shock reformation and implication for shock surfing, *J. Geophys. Res.*, *108*, 1014–1024, doi: 10.1029/2002JA009515.

Shimada, N., and M. Hoshino (2000), Strong electron acceleration at high Mach number shock waves: Simulation of electron dynamics, *Astrophys. J.*, *543*, L67–L71.

Shimada, N., and M. Hoshino (2004), Electron heating and acceleration in the shock transition region: Background plasma parameter dependence, *Phys. Plasma*, *11*, 1840–1849.

Umeda, T., Y. Kidani, S. Matsukyio, and R. Yamazaki (2012), Modified two-stream instability at perpendicular collisionless shocks: Full particle simulations, *J. Geophys. Res.*, *117*, A03206, doi:10.1029/2011JA017182.

Usui, H., W. Paterson, H. Matsumoto, L. Franck, M. Nakamura, H. Matsui, T. Yamamoto, O. Nishimura, and J. Koizumi (1999), Geotail electron observations in association with intense bursts of electron cyclotron harmonics waves in the dayside magnetosphere, *Geophys. Res.*, *104*, A3, doi:10.1029/1998JA900151.

Wilson III, L. B., C. A. Cattell, P. J. Kellogg, K. Goetz, K. Kersten, J. C. Kasper, A. Szabo, and M. Wilber (2010), Large-amplitude electrostatic waves observed at a supercritical interplanetary shock, *J. Geophs. Res.*, *115*, A12104, doi:10.1029/2010JA015332.

Wong, H. V. (1970), Electrostatic electron-ion streaming instability, *Phys. Fluids*, *13*, 757–760.

Wu, C. S., et al. (1984), Microinstabilities associated with a high Mach number, perpendicular bow shock, *Space Science Rev.*, *37*, 63–109.